Growth of ZIF-8 Nanoparticles In Situ on Graphene Oxide Nanosheets: A Multifunctional Nanoplatform for Combined Ion-Interference and Photothermal Therapy

Chunxu Lv, Wenyan Kang, Shuo Liu, Pishan Yang, Yuta Nishina, Shaohua Ge, Alberto Bianco, Baojin Ma

Growth of ZIF-8 Nanoparticles *in Situ* on Graphene Oxide Nanosheets: A Multifunctional Nanoplatform for Combined Ion-interference and Photothermal Therapy

Chunxu Lv,[&,#] *Wenyan Kang,*[&,#] *Shuo Liu,*[&] *Pishan Yang,*[&] *Yuta Nishina,*[§] *Shaohua Ge,*[&,*] *Alberto Bianco,*[$,*] *Baojin Ma*[$,&,*]

[&]*Department of Periodontology & Tissue Engineering and Regeneration, School and Hospital of Stomatology, Cheeloo College of Medicine, Shandong University & Shandong Key Laboratory of Oral Tissue Regeneration & Shandong Engineering Laboratory for Dental Materials and Oral Tissue Regeneration, Jinan, Shandong, 250012, China*

[§]*Graduate School of Natural Science and Technology, Okayama University, Tsushimanaka, Kita-ku, Okayama, 700-8530, Japan; Research Core for Interdisciplinary Sciences, Okayama University, Tsushimanaka, Kita-ku, Okayama, 700-8530, Japan*

[$]*CNRS, Immunology, Immunopathology and Therapeutic Chemistry, UPR3572, University of Strasbourg, ISIS, Strasbourg, 67000, France*

Correspondence to:

Shaohua Ge: shaohuage@sdu.edu.cn; Alberto Bianco: a.bianco@ibmc-cnrs.unistra.fr; Baojin Ma: baojinma@sdu.edu.cn

ABSTRACT: The regulation of intracellular ions' overload to interrupt normal bioprocesses and cause cell death has been developed as an efficient strategy (named as ion-interference therapy/IIT) to treat cancer. In this study, we design a multifunctional nanoplatform (called BSArGO@ZIF-8 NSs) by *in situ* growth of metal organic framework nanoparticles (ZIF-8 NPs) onto the graphene oxide (GO) surface, subsequently reduced by ascorbic acid and modified by bovine serum albumin. This nanocomplex causes the intracellular overload of Zn^{2+}, an increase of reactive oxygen species (ROS), and exerts a broad-spectrum lethality to different kinds of cancer cells. BSArGO@ZIF-8 NSs can promote cell apoptosis by initiating bim (a pro-apoptotic protein)-mediated mitochondrial apoptotic events, up-regulating PUMA/NOXA expression, and down-regulating the level of Bid/p53AIP1. Meanwhile, Zn^{2+} excess triggers cellular dysfunction and mitochondria damage by activating the autophagy signaling pathways and disturbing the intracellular environmental homeostasis. Combined with the photothermal effect of reduced GO (rGO), BSArGO@ZIF-8 NSs mediated ion-interference and photothermal combined therapy leads to effective apoptosis and inhibits cell proliferation and angiogenesis, bringing a higher efficacy in tumor suppression *in vivo*. This designed Zn-based multifunctional nanoplatform will allow promoting further the development of IIT and the corresponding combined cancer therapy strategy.

Keywords: carbon nanomaterials, zinc ions, metal organic framework, mitochondria, phototherapy

INTRODUCTION

Various ions (*e.g.* Ca^{2+}, Zn^{2+}, Na^{+}) are present inside the cells and participate in many important reactions, which are crucial to maintaining normal cellular functions and behaviors.[1-3] For example, as one of the most important signaling factors, Ca^{2+} can regulate muscle contraction, neuronal excitability, cell migration, and growth.[4] As a cofactor, Fe can regulate oxygen transport, cellular respiration, DNA synthesis, and cellular energy metabolism.[5] However, when the level of intracellular ions overloads, many physiological processes are interrupted, causing cell dysfunctions and even death.[6-8] Based on these mechanisms, bioactive materials-mediated ion-interference therapy (IIT) has been developed as a promising strategy to treat cancer.[9,10] A series of interesting studies reporting different IIT strategies appeared very recently.[11-15] By interfering with osmotic pressure, disturbing cellular communication, activating biocatalysis, and targeting DNA/proteins, IIT possesses relatively high efficacy in cancer therapy. IIT is usually based on biodegradable and nontoxic elements, which endow this strategy with low systemic toxicity and high biosafety. A typical representative application is based on Ca^{2+} overload.[16-18] Sodium hyaluronate-modified calcium peroxide-based nanoparticles can efficiently release Ca^{2+} intracellularly in an acidic environment, bringing to cancer cell death and tumor calcification.[19] To further amplify intracellular Ca^{2+} excess, $CaCO_3$ nanoparticles incorporated with Kaempferol-3-O-rutinoside (which can disrupt calcium homeostasis regulation and facilitate calcium influx) were prepared to improve the efficiency of the treatment.[20] Alternatively, NaCl nanoparticles were used to cause a surge of osmolarity and rapid cell lysis, leading to cancer cell death.[21] However, these complex nanomaterials for IIT often aggregate and are not stable in physiological conditions. For example, $CaCO_3$ nanoparticles easily recrystallize growing into big particles, while NaCl nanoparticles are dissolved when exposed to water and the physiological environment. To maintain the stability and dispersibility of nanomaterials, an appropriate surface modification is necessary, which however generally causes high cost, low productivity, cumbersome preparation processes, and short storage cycles. Therefore, designing a nanoplatform with relatively high stability in physiological conditions is crucial to promote IIT development.

Zn^{2+} is an essential cofactor in many enzymes and regulatory proteins.[22,23] Similarly to Ca^{2+}, excess of Zn^{2+} can break intracellular homeostasis, causing an increase of the level of reactive oxygen species (ROS),[24] mitochondrial damage, and cell apoptosis.[25,26] Therefore, efficiently increasing the

intracellular Zn^{2+} level will show high lethality to cancer cells based on Zn^{2+}-mediated IIT. Degradable zeolitic imidazolate framework-8 (ZIF-8), made of Zn^{2+} and 2-methylimidazole, can serve as an efficient Zn^{2+} source due to the pH-sensitive performance, which makes it an efficient carrier for drug delivery.[27-31] However, the hydrophobicity, high crystallinity, and relatively big size of ZIF-8 will limit a rapid accumulation of a high concentration of intracellular Zn^{2+}.[28,32,33] Graphene oxide (GO) is very popular as a promising carrier due to its good biocompatibility and biodegradability and can serve as a suitable template for the growth of nanoparticles.[34-37] The nucleation points on GO can guide the nanomaterial formation and restrict aggregation of formed nanomaterials, leading to a well-dispersed and small-sized complex on the GO surface. Furthermore, GO and reduced GO (rGO) have been widely applied in photothermal therapy (PTT).[38,39] PTT is a non-invasive and controllable strategy with minimal side effects to eliminate tumor cells exploiting the photothermal effect mediated by agents such as carbon nanomaterials, metal nanocrystals, metal-based nanomaterials, transition metal dichalcogenides, Xenes, Mxenes, and others.[40-42] Due to the excellent photothermal effect, low cost, and high biocompatibility, GO-based materials have attracted much attention.[43,44] Therefore, the design of a zinc-based nanoplatform for IIT by *in situ* growth of ZIF-8 onto GO surface might result in a straightforward strategy to achieve a satisfactory photothermal therapeutic efficiency. Indeed, a recent study has designed ZIF-8/GQD (GQDs, graphene quantum dots) for cancer therapy by photothermal effect and drug delivery.[45] As an alternative, rGO not only shows a high photothermal effect but also works better as a template for ZIF-8 NPs *in situ* growth. Indeed, rGO could serve as a larger size carrier compared to GQDs to increase the content of ZIF-8 NPs in cells, showing a high lethality in cancer cells, as we recently proved for MnO_2 NPs.[46]

As ZIF-8 was seldom used to treat cancer exploring mediated ion interference,[13] we conceived, here, a multifunctional nanoplatform based on *in situ* growth of ZIF-8 NPs onto GO sheets to treat oral cancers. Oral cancer is the sixth most common malignant tumor in the world, with a high mortality rate, posing a great threat to people's health.[47,48] Therefore, we decided to select oral cancer-related cell lines and Cal27 subcutaneous tumor model. Furthermore, to confirm the broad-spectrum lethality of BSArGO@ZIF-8 NSs, HeLa cells (the most commonly used cancer cell model) were also used. To increase the photothermal effect of our system, GO was reduced to rGO by ascorbic acid (Vitamin C, Vc), followed by modification of rGO@ZIF-8 nanosheets with bovine serum albumin (BSA).

Consequently, BSArGO@ZIF-8 NSs could exert a broad-spectrum high lethality to different kinds of cancer cells by causing the intracellular Zn^{2+} overload and ROS increase. BSArGO@ZIF-8 NSs could initiate bim (a pro-apoptotic protein)-mediated mitochondrial apoptotic events and promote cell apoptosis. Meanwhile, the overloaded intracellular Zn^{2+} could trigger cellular dysfunctions and mitochondrial damage. Furthermore, BSArGO@ZIF-8 NSs had higher lethality to cancer cells under NIR irradiation. Compared with BSArGO@ZIF-8 NSs alone, BSArGO@ZIF-8 NSs mediated ion-interference and photothermal combined therapy caused apoptosis more effectively and inhibited cell proliferation and angiogenesis, bringing a higher efficacy of tumor suppression.

RESULTS AND DISCUSSION

Synthesis and characterization of BSArGO@ZIF-8 NSs. GO@ZIF-8 NSs were prepared in a methanol solution by a modified method based on a previous report (**Figure 1**a).[49] To obtain a better photothermal effect and stability, GO@ZIF-8 NSs were reduced by Vc and modified by BSA to form BSArGO@ZIF-8 NSs. After reduction of GO by Vc, the color changed from light brown to dark brown (**Figure S1**). Raman spectra showed an increased value of I_D/I_G ratio (**Figure 1**b and c) in rGO@ZIF-8 and BSArGO@ZIF-8 NSs, meaning that the number of smaller graphitic domains in GO increased after treating with Vc, similarly to previous reports,[46,50,51] supporting the formation of rGO. The XRD pattern of rGO@ZIF-8 NSs (**Figure S2**) showed typical diffraction peaks of ZIF-8. The intensity of diffraction peaks is relatively weak, meaning the formed ZIF-8 has low crystallinity.[52] After the modification with BSA, BSArGO@ZIF-8 NSs presented only a weak diffraction peak (211) of ZIF-8 at around $2\theta = 13°$ and the characteristic peak of BSA at around 22°.[53] Furthermore, the FT-IR spectrum of rGO@ZIF-8 NSs presents the typical absorption peaks of ZIF-8 (**Figure S3**).[32,54] After adding BSA, the FT-IR spectrum of BSArGO@ZIF-8 shows the strong absorption peaks of BSA, weakening the absorption peaks of ZIF-8. This is a clear sign that rGO@ZIF-8 NSs have been modified by BSA to form BSArGO@ZIF-8 NSs.

rGO@ZIF-8 NSs were easily dispersed and resulted in stable dispersion in methanol (**Figure S4**), and ZIF-8 NPs homogeneously grew on the surface of GO (**Figure 1**e and f) with a size of about 21 nm. When rGO@ZIF-8 NSs were transferred from methanol into PBS, aggregation appeared immediately (**Figure S4**a-d). However, after the modification with BSA, BSArGO@ZIF-8 NSs gained

a high stability in PBS (**Figure S4**a), with almost no aggregation even after 48 h (**Figure S4**d). The size of BSArGO@ZIF-8 NSs, measured by dynamic light scattering (DLS), was ~800 nm, and the size distribution of the particles did not change after being dispersed in PBS for 24 h (**Figure S5**). The value of zeta potential of BSArGO@ZIF-8 NSs dispersed in PBS resulted -10.41 mV, similar to BSA-modified ZIF-8 NPs previously reported.[55] After 24 h, the value of zeta potential of BSArGO@ZIF-8 NSs was -8.98 mV. Therefore, the results of DLS and zeta potential confirmed that BSArGO@ZIF-8 NSs possess a relatively high colloidal stability. Transmission electron microscope (TEM) image of BSArGO@ZIF-8 NSs also confirmed the excellent dispersibility in aqueous solution (**Figure 1**g). Meanwhile, the imaging of ZIF-8 NPs became a little blurred in the high-resolution TEM image (**Figure 1**h), likely due to BSA coating on the surface of rGO@ZIF-8 NSs. *In situ* growth strategy can limit the formation of big-size particles of ZIF-8, which could be attributed to the favorable interaction between GO and ZIF-8.[56,57] We have seen instead that in the absence of GO, BSAZIF-8 can easily aggregate to form particles of big size (**Figure S6**). XPS results also demonstrated that ZIF-8 NPs grew on the surface of GO (**Figure 1**i). Due to the surface modification by BSA, the atomic ratio of zinc is lower in BSArGO@ ZIF-8 NSs than that in rGO@ZIF-8 NSs. Therefore, compared to rGO@ZIF-8 NSs, the signal intensity of Zn in BSArGO@ZIF-8 NSs obviously decreased, confirming that rGO@ZIF-8 NSs were modified by BSA. The valence state of zinc was +2 according to the high-resolution XPS spectra of Zn2p, which is consistent with other studies.[58,59] Furthermore, according to the weight change from GO to GO@ZIF-8, the loading content of ZIF-8 onto GO was ~15.1 mg (ZIF-8) per 1 mg (GO), showing a high loading efficiency of GO.

In addition, BSArGO@ZIF-8 NSs adsorbed at 808 nm (**Figure S7**a), a characteristic that accounts for an increase of temperature of a 200 μg/mL dispersion of about 30 ℃ under NIR irradiation (at 1 W/cm^2) for 10 min (**Figure S7**b). According to the calculation, the photothermal conversion efficiency was ~22.5%.[60] Therefore, BSArGO@ZIF-8 NSs possess good photothermal effect.[61] Meanwhile, the absorption intensity of BSArGO@ZIF-8 NSs at 808 nm was almost the same before and after being dispersed in PBS for 24 h, meaning that the photothermal effect remains stable overtime. It has been previously demonstrated that ZIF-8 can release Zn^{2+} efficiently in acid conditions rather than in the neutral ambience, meaning that ZIF-8 possesses a responsive release property in the tumor cell microenvironment.[13,30] The values of Zn^{2+} release at different pH measured by ICP-MS supported a similar conclusion (**Figure S8)**. Only little Zn^{2+} was released after 24 h when pH values were 7.4 and

6.5. However, most of Zn^{2+} was released after 24 h at pH 5.0. This result confirmed that BSArGO@ZIF-8 NSs can increase the intracellular Zn^{2+} level efficiently after being internalized by cancer cells.

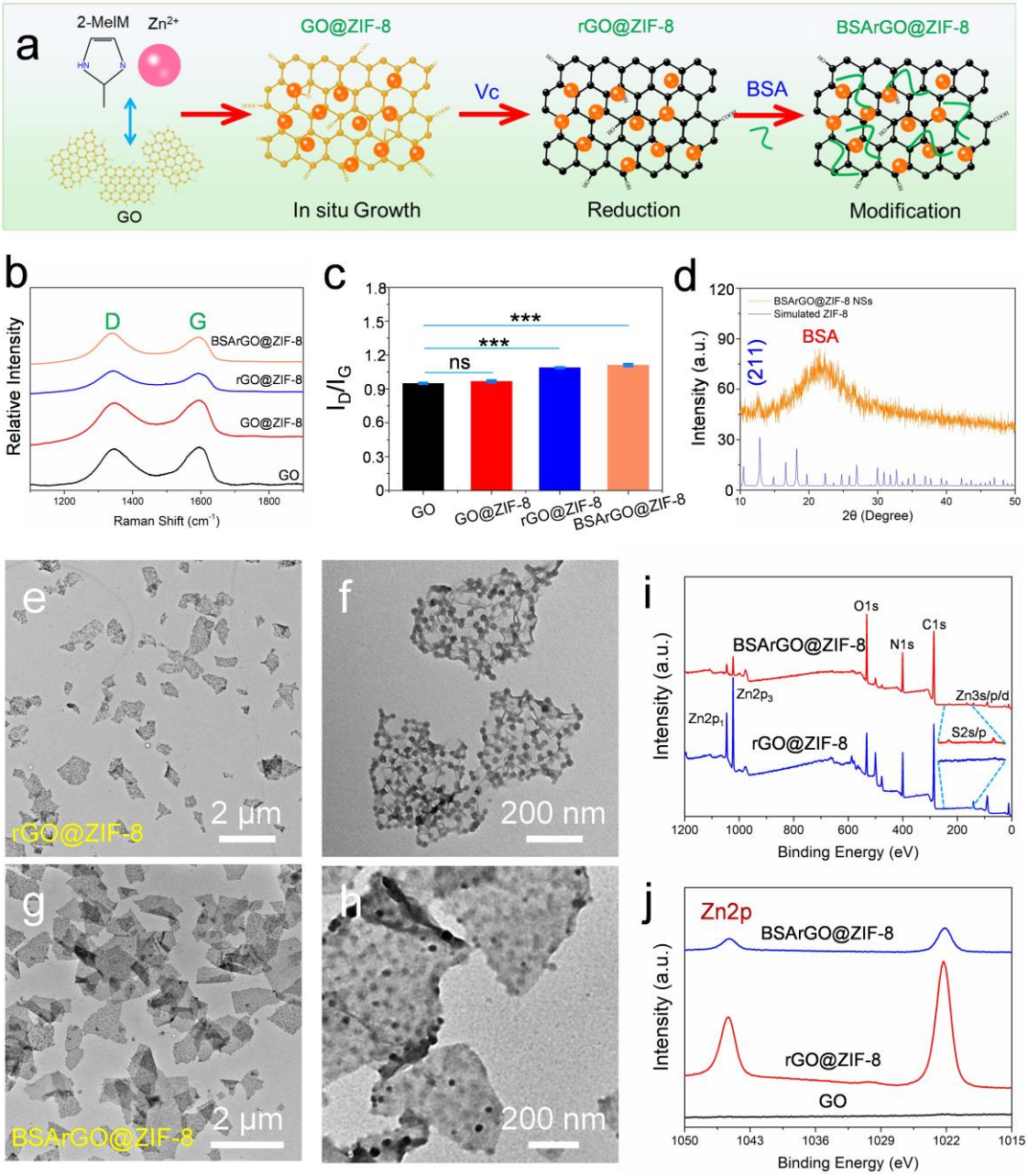

Figure 1. Preparation and characterization of BSArGO@ZIF-8 NSs. a) Schematic preparation of BSArGO@ZIF-8 NSs. b, c) Raman spectra and I_D/I_G ratio. d) XRD pattern of BSArGO@ZIF-8 NSs. e,f) TEM images of rGO@ZIF-8 NSs at different magnifications. g, h) TEM images of BSArGO@ZIF-8 NSs at different magnification. i) XPS full spectra of rGO@ZIF-8 and BSArGO@ZIF-8 NSs. j) High-resolution XPS spectra to confirm Zn valence state.

Lethality of BSArGO@ZIF-8 NSs to cancer cells. Following the preparation and characterization of our system, we started to explore the biological effects. The viability of different types of cancer cell lines treated with BSArGO@ZIF-8 NSs was measured using the cell counting kit-8 (CCK-8) assay. The different cancer cells showed different tolerance to BSArGO@ZIF-8 NSs. When the concentration of BSArGO@ZIF-8 NSs was above 200 μg/mL, the viability of HeLa and SCC25 cells obviously decreased after 24 h and 48 h (**Figure 2**a and b). However, there was almost no effect on the viability when the concentration of BSArGO@ZIF-8 NSs was below 150 μg/mL. For Cal27 and HN4 cells, BSArGO@ZIF-8 NSs had high lethality at 150 μg/mL concentration and almost no effect below 100 μg/mL. The differences in the effective concentrations should attribute to the different resistance of the cells to Zn^{2+}, similarly to a previous report.[62] Meanwhile, due to the self-regulation ability, cells were able to keep a high viability within a specific concentration range of BSArGO@ZIF-8 NSs, by maintaining intracellular Zn^{2+} homeostasis.[63,64] However, when the intracellular Zn^{2+} was out of tolerance, the cells tended to die. We also performed the live/dead staining for SCC25 and Cal27 cells to show the cell state changes after BSArGO@ZIF-8 NSs treatment. In the control group, there were almost no dead cells. After incubating the cells with BSArGO@ZIF-8 NSs, a lot of dead cells appeared, with few cells still alive. These results indicate that BSArGO@ZIF-8 NSs possess a high broad-spectrum lethality to different kinds of cancer cells at the efficient concentrations. Furthermore, GO and rGO had almost no effect on the viability of Cal27 cells at an equivalent concentration (**Figure S9** and **S10**), excluding a cytotoxic contribution to cell death. BSAZIF-8 did also almost not affect cells viability (**Figure S11**), likely due to the big size of BSAZIF-8 particles, hampering their internalization by cancer cells and consequently making them inefficient to provoke ion interference. Meanwhile, the toxicity of BSArGO@ZIF-8 NSs to normal cells (bone mesenchymal stem cells/BMSCs and bone marrow stromal cells/ST2 cells) was measured **(Figure S12**). At concentrations below 200 μg/mL, the viability of BMSCs was slightly affected at both time points analyzed, while the viability of ST2 cells decreased to ~69% only at 200 μg/mL after 48 h. When the concentration was increased to 400 μg/mL, BSArGO@ZIF-8 NSs resulted very toxic for both types of cells, although it is unlikely that such a huge dose is used for cancer therapy. In general, compared with the toxicity to cancer cells, BSArGO@ZIF-8 NSs possess relatively high biocompatibility to normal cells at cancer therapeutic effective concentrations.

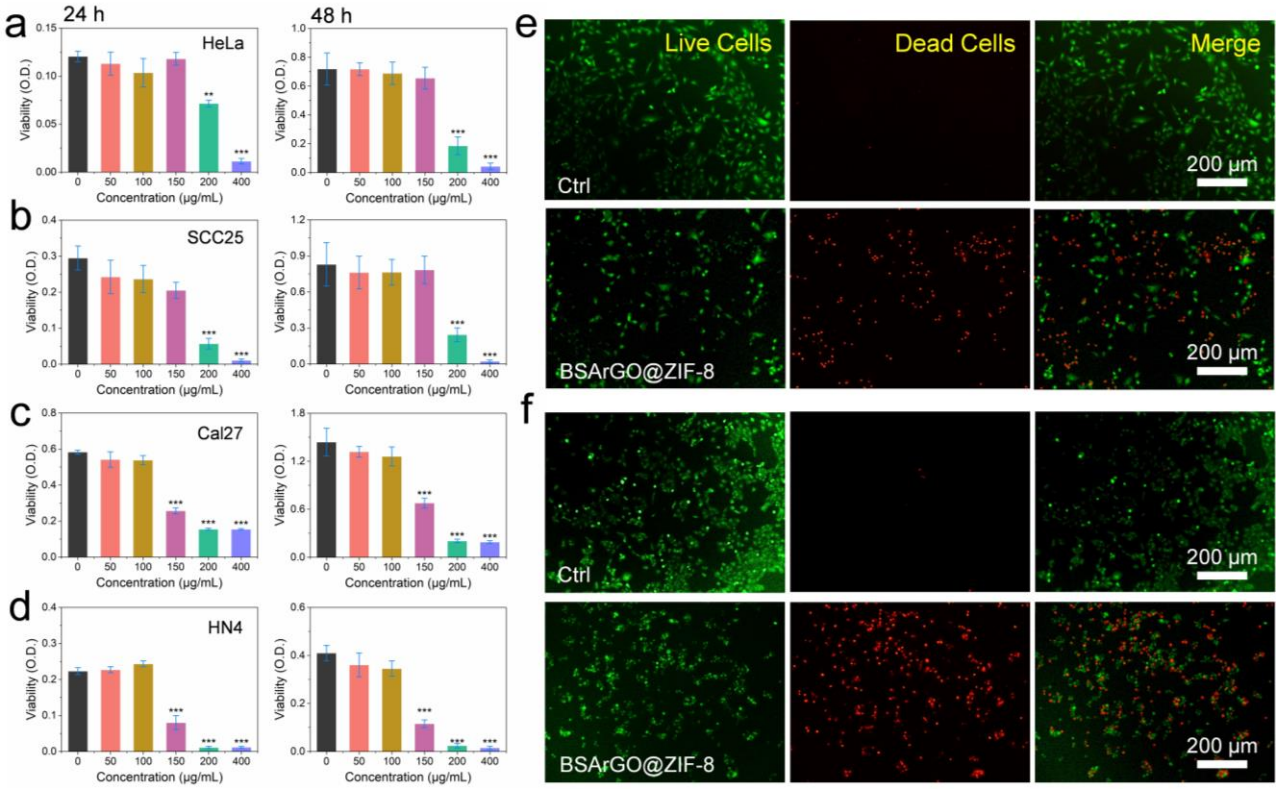

Figure 2. Lethality of BSArGO@ZIF-8 NSs towards different cancer cells. a-d) Viability of HeLa, SCC25, Cal27 and HN4 cells treated with BSArGO@ZIF-8 NSs at different concentrations. e, f) Live/dead staining of SCC25 and Cal27 cells treated with BSArGO@ZIF-8 NSs (200 μg/mL and 150 μg/mL, respectively) after 24 h.

Intracellular increase of Zn^{2+} and ROS produced by BSArGO@ZIF-8 NSs. To confirm the changes in the content of intracellular Zn^{2+} after BSArGO@ZIF-8 NSs treatment, we used 6-[2-[bis(2-pyridylmethyl)amino]ethylamino]-2′,7′-difluorofluorescein diacetate (ZnAF-2) as a probe to measure the amount of Zn^{2+} by fluorescence staining. The fluorescence intensity of ZnAF-2 is almost zero without Zn^{2+}. With the increased Zn^{2+} concentration, the fluorescence signal augments synchronously.[65] The fluorescence intensity clearly increased in SCC25, Cal27 and HeLa cells after incubation with BSArGO@ZIF-8 NSs (**Figure 3**a and c, **Figure S13**a). The relative fluorescence intensity of Zn^{2+} in SCC25, Cal27 and HeLa cells treated with BSArGO@ZIF-8 NSs was ~10 folds, ~5 folds, and ~10 folds in comparison to the control group, respectively. For a more accurate quantitative analysis, flow cytometry analysis was performed. After BSArGO@ZIF-8 NSs treatment, the fluorescence intensity of intracellular Zn^{2+} increased to ~30 folds in SCC25 cells, ~60 folds in Cal27 cells, and ~64 folds in HeLa cells, respectively (**Figure 3**b and d, **Figure S13**b). Therefore, after

being internalized by cancer cells, BSArGO@ZIF-8 NSs can efficiently increase intracellular Zn^{2+} content.

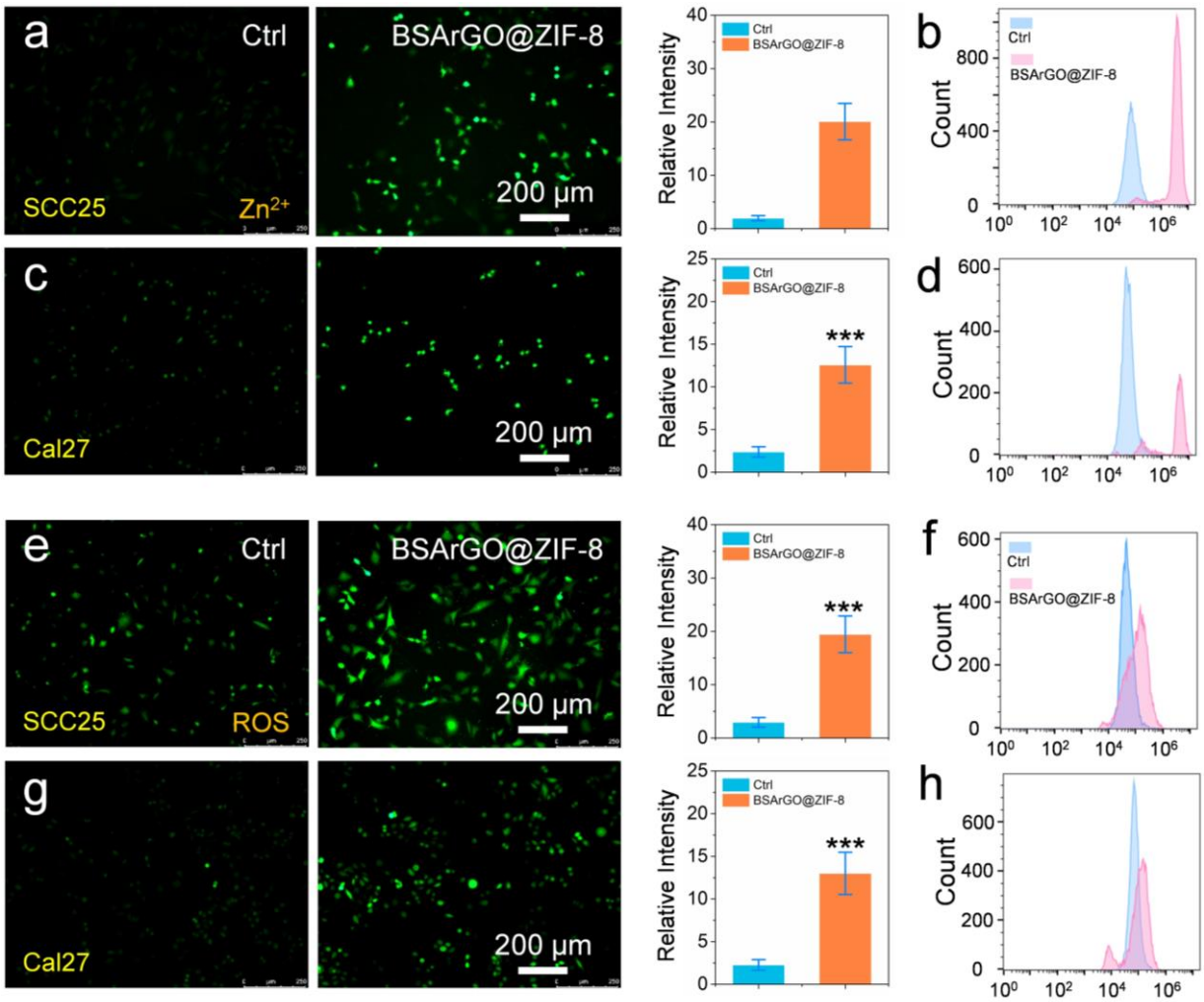

Figure 3. Intracellular Zn^{2+} content and ROS level change after BSArGO@ZIF-8 NSs treatment. a) Fluorescence detection and b) flow cytometry analysis of Zn^{2+} level in SCC25 cells treated with BSArGO@ZIF-8 NSs at 200 μg/mL after 6 h. c) Fluorescence detection and d) flow cytometry analysis of Zn^{2+} level in Cal27 cells treated with BSArGO@ZIF-8 NSs at 150 μg/mL after 6 h. e) Fluorescence detection and f) flow cytometry analysis of ROS level in SCC25 cells treated with BSArGO@ZIF-8 NSs at 200 μg/mL after 6 h. g) Fluorescence detection and h) flow cytometry analysis of ROS level in Cal27 cells treated with BSArGO@ZIF-8 NSs at 150 μg/mL after 6 h.

The excess of Zn^{2+} content usually causes an increase of ROS level.[66] 2',7'-Dichlorodihydrofluorescein diacetate (H2DCFDA) probe was used to detect this change. Consistent

with Zn^{2+} content modification, ROS level significantly increased after BSArGO@ZIF-8 NSs treatment, and the relative fluorescence intensity of ROS in SCC25, Cal27 and HeLa cells treated with BSArGO@ZIF-8 NSs was ~7 folds, ~6 folds, and ~8 folds in respect to the control group (**Figure 3**e and g, **Figure S13**c). Similarly, flow cytometry was performed to obtain a more accurate quantitative analysis. After BSArGO@ZIF-8 NSs treatment, the fluorescence intensity of ROS probe increased to ~3 folds in SCC25 cells, ~2 folds in Cal27 cells, and ~2 folds in HeLa cells, respectively (**Figure 3**f and h, **Figure S13**d). From these data, it is clear that BSArGO@ZIF-8 NSs can cause an enhanced intracellular ROS production due to a dysregulation of the intracellular Zn^{2+} content. To further confirm the uptake and cell internalization of BSArGO@ZIF-8 NSs, lysosomal colocalization staining was performed. As shown in **Figure S14**, most of the fluorescence signals overlapped. Due to the diffusion of Zn^{2+} released from ZIF-8, the green fluorescence had a wider distribution than only inside lysosomes. Therefore, the cell internalization of BSArGO@ZIF-8 NSs is likely following the lysosome pathway, which is consistent with a previous report.[67]

Mechanism of BSArGO@ZIF-8 NSs to kill cancer cells. To accurately clarify the mechanism of BSArGO@ZIF-8 NSs causing cancer cell death, the whole transcriptome sequencing of Cal27 cells treated with or without BSArGO@ZIF-8 NSs was performed. The results of the Pearson correlation analysis showed that BSArGO@ZIF-8 could significantly vary the gene expression inside the cells, and duplicates of three independent experiments were highly consistent (**Figure 4**a). The difference generated by BSArGO@ZIF-8 NSs was further confirmed by the principal component analysis (PCA) (**Figure S15**a). Differentiated expressed genes (DEGs) were identified according to the threshold value of $|Log2FC| \geq 1$ and false discovery rate (FDR) ≤ 0.05. The Volcano plot showed that 1091 DEGs were up-regulated and 1136 DEGs were down-regulated. The top 20 genes, such as CCN2, FOS, MT1X are highlighted in **Figure 4**b, while the proportions of up- and down-regulating DEGs are shown by the pie chart (**Figure S15**b). The results of Gene Ontology analysis showed that these DEGs were involved in the apoptotic process, cell cycle (biological process), mitochondria, cytoskeleton (cellular component), and metal ion binding, and DNA binding (molecular function) were significantly enriched (**Figure S16**). In addition, the Scatter Plot based on the Gene Ontology database showed that part of the DEGs caused by BSArGO@ZIF-8 NSs were significantly enriched in DNA binding-related signaling pathways, which indicated that BSArGO@ZIF-8 NSs regulate Cal27 cell proliferation and

apoptosis by influencing the activity of intracellular DNA (**Figure 4**c). Furthermore, the Kyoto Encyclopedia of Genes and Genomes (KEGG) enrichment analysis allowed identifying that a total of 63 DEGs were involved in cell growth and death signaling pathways (cellular processes), and more than 100 DEGs were associated with cancer-related signaling pathways (human diseases). In addition, other metabolism signaling pathways such as amino acid metabolism and energy metabolism signaling pathways were highly associated with cell proliferation and apoptosis (**Figure 4**d).[68,69] The heatmap presented each gene expression level enriched in cell growth and disease, and cancer-specific pathways (**Figure S17**). The results indicate that the gene level of FOS, JUN, CXCL8 was significantly increased, while the expression of BIRC3, NFKBIA and SMAD3 were decreased, confirming that they play important roles in cancer cell growth and death. [68,69]

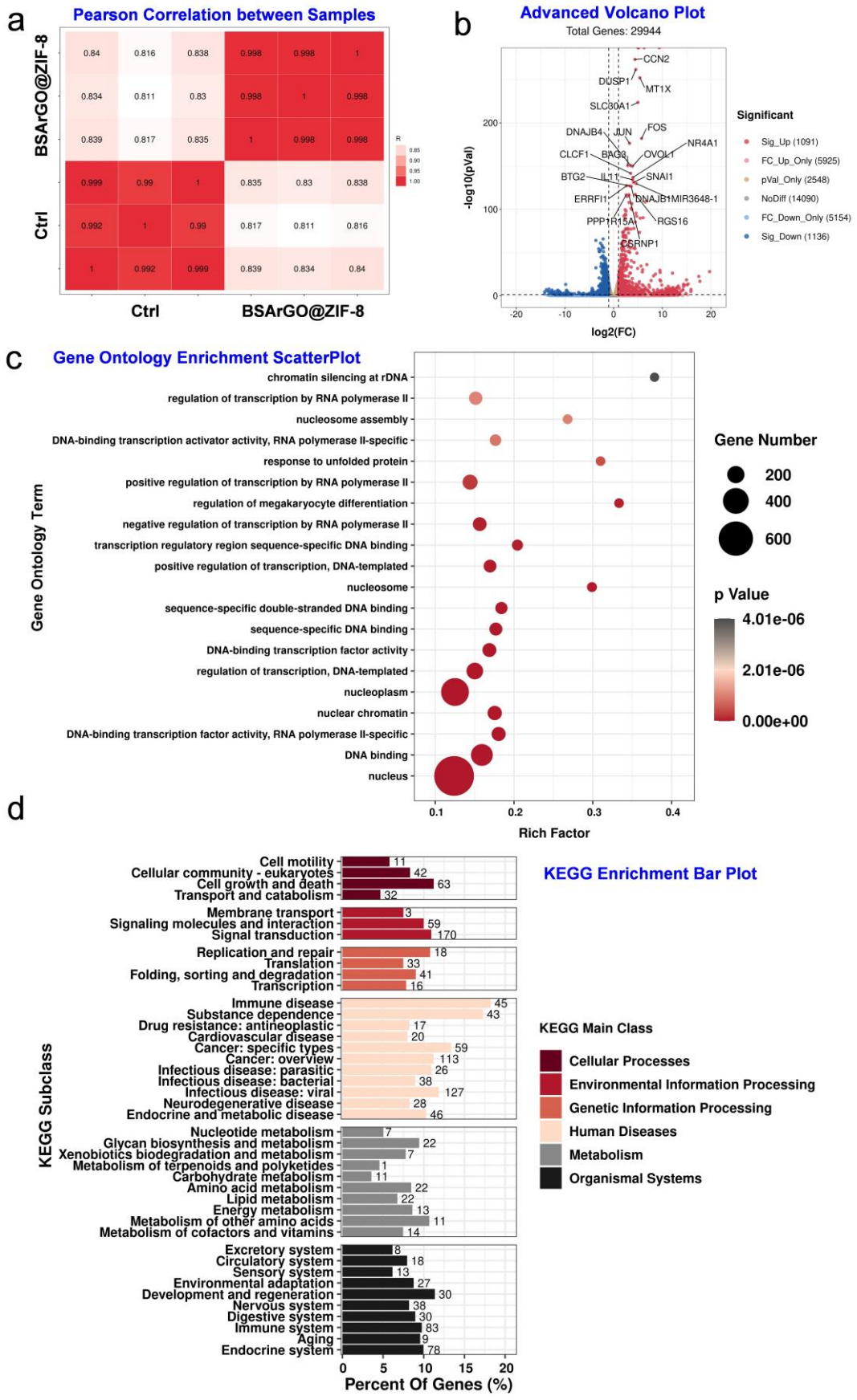

Figure 4. Lethality mechanism to cancer cells of BSArGO@ZIF-8 NSs based on RNA-seq analysis. a) Pearson correlation analysis of Cal27 cells with or without BSArGO@ZIF-8 NSs treatment. b)

DEGs in Cal27 cells with or without BSArGO@ZIF-8 NSs treatment (|Log2FC| ≥ 1 and q < 0.05). c) Gene Ontology enrichment analysis of DEGs by bubble diagram. d) KEGG enrichment analysis of DEGs presented by bar diagram.

To further explore the molecular mechanism of BSArGO@ZIF-8 NSs promoted Cal27 apoptosis, we use a series of varied methods to screen the apoptosis-related signaling pathways and genes. The bubble diagram based on KEGG enrichment analysis demonstrated that these DEGs were significantly enhanced in cell cycle, apoptosis pathway, mitogen-activated protein kinase (MAPK) signaling pathways (**Figure 5**a), which have been confirmed to play key roles in regulating cancer cell growth and apoptosis.[70-72] The heatmap showed that DEGs enriched in apoptosis signaling pathways were constituted of 11 up-regulated DEGs and 9 down-regulated DEGs, including for example Mcl1, FOS, JUN, CASP12, CASP2, BIRC3, and TNFRSF1A (**Figure 5**b).[73-78] The Pathview analysis demonstrated that BSArGO@ZIF-8 NSs alter most genes in apoptosis-related signaling pathways, including down-regulation of α-tubulin, PARP, Lamin, TRAIL, TNF-R1, FADD, and CASP10, and up-regulating JNK and Mcl-1 (**Figure 5**c). In addition, BSArGO@ZIF-8 NSs could change pro-apoptotic gene expression, up-regulating Fas-L, Bim, HRK, and down-regulating Fas. We also found that BSArGO@ZIF-8 NSs could activate bim-mediated mitochondrial apoptotic events by increasing Mcl-1 expression, induce disruption of microtubule function, provoke the loss of integrity of the nuclear membrane and lead to DNA fragmentation by up-regulating Bim and NOXA, and down-regulating Bak and Bcl-2. Our results confirmed that BSArGO@ZIF-8 NSs could also significantly activate autophagy and cancer signaling pathways (**Figure S18** and **S19**). In addition, gene set enrichment analysis (GSEA) was used to select the apoptosis-related signaling pathways and genes. In particular, we focused on apoptosis in multiple species and cellular Zn^{2+} homeostasis signaling pathways, which were significantly associated with cell apoptosis (**Figure 5**d).[79] GSEA results also indicated that BSArGO@ZIF-8 NSs generated DEGs were significantly enriched in the cellular response to Zn^{2+} and cell cycle signaling pathways (**Figure S20** and **S21**). According to GSEA results, we identified that the genes expression of FADD, BIRC3, TNFRSF1A, BCL2, and CASPASE7 significantly decreased, while the gene expression of BCL2L11, CYCS, BBC3, and CASP9 clearly increased, synergistically promoting cell apoptosis (**Figure 5**e).[80,81] We eventually found that the

genes in MT1 and SLC families were mainly involved in regulating cellular Zn^{2+} homeostasis (**Figure 5**e). Intracellular high concentration of Zn^{2+} could directly induce cell death and could also indirectly kill cells by altering the tumor microenvironment.[82]

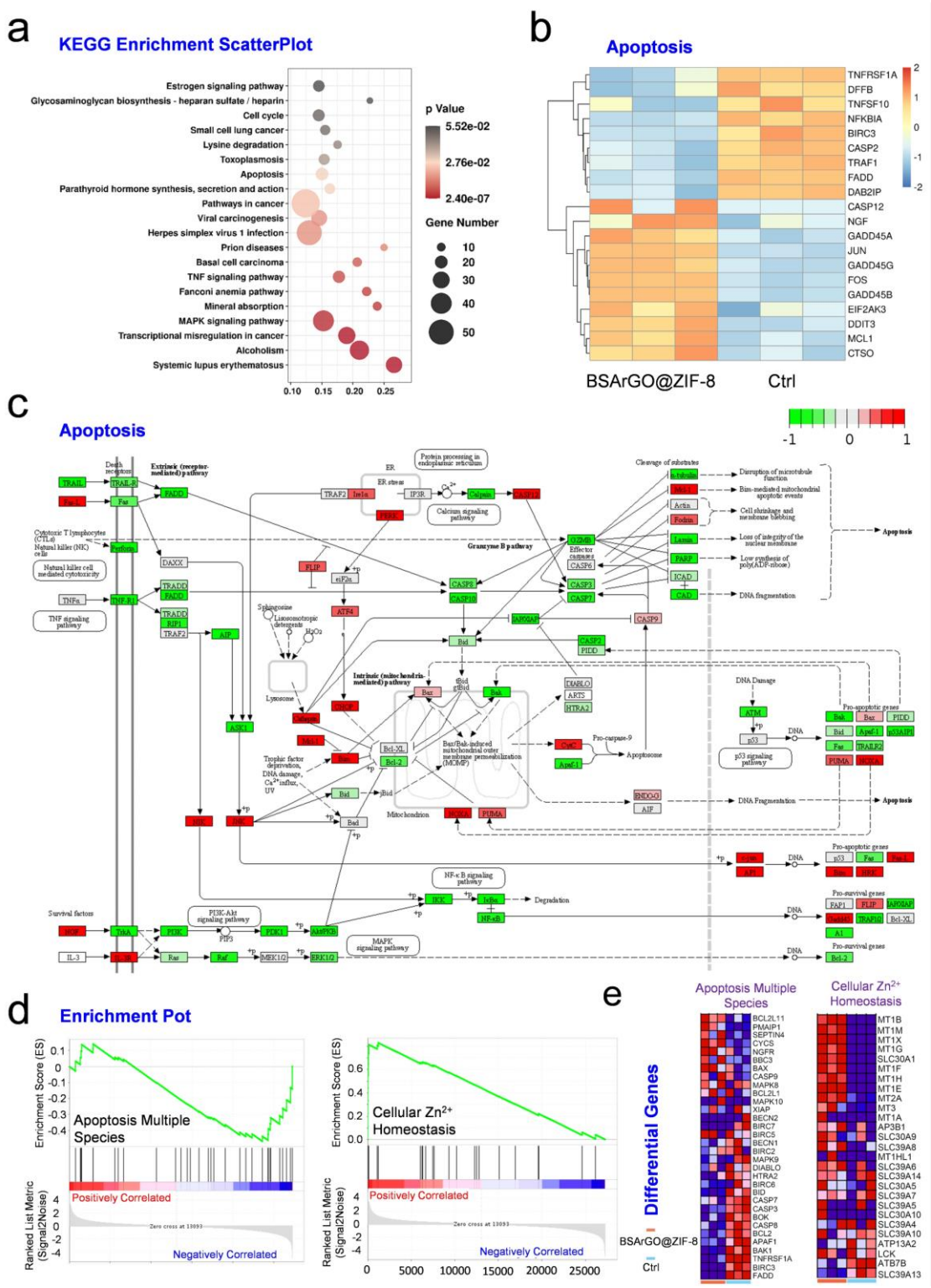

Figure 5. Apoptosis molecular mechanism of Cal27 cells after BSArGO@ZIF-8 NSs treatment. a) KEGG enrichment analysis of DEGs in BSArGO@ZIF-8 NSs intracellular delivery presented by

bubble diagram. b) Heatmap apoptosis associated DEGs. c) Pathview analysis of apoptosis signaling pathway based on KEGG database. The red boxes represent up-regulated genes, and the green boxes represent downregulated genes. d) Apoptosis multiple species and cellular zinc ion homeostasis signaling pathways based on GSEA. e) Heatmap apoptosis associated DEGs and the Zn^{2+} action associated DEGs.

Cell apoptosis and mitochondrial damage caused by BSArGO@ZIF-8 NSs. Based on RNA-seq analysis, cell apoptosis and mitochondrial damage are the main two events caused by the excess of Zn^{2+}. Cell apoptosis was observed by fluorescence microscope. Both numbers of Annexin V-labeled early apoptotic cells and PI-labeled late apoptotic cells significantly increased after being treated with BSArGO@ZIF-8 NSs, compared with the control group (**Figure 6**a-c). It is worth noting that late apoptotic cells were evidently more than early apoptotic cells. Quantitative analysis of cell apoptosis was also performed by flow cytometry. After BSArGO@ZIF-8 NSs treatment, the percentage of late apoptotic cells increased to 62.2% from 2.7%, and the percentage of early apoptotic cells increased to 10.1% from 1.2%, compared with the control group. The proportion of late apoptotic cells was about 6 folds as that of early apoptotic cells, consistent with the results of immunofluorescence staining. The decrease of mitochondrial membrane potential is a landmark event in the early stage of cell apoptosis.[83] Upon the apoptosis came up and Zn^{2+} excessed, the potential of mitochondrial membrane would decrease and JC-1 (5,5′,6,6′-tetrachloro-1,1′,3,3′-tetraethyl-imidacarbocyanine, a mitochondrial membrane potential probe) would lose the ability to aggregate in mitochondria and form monomers. Through immunofluorescence staining, the results confirmed that BSArGO@ZIF-8 NSs could significantly reduce the polymer production in the mitochondrial matrix and increase the formation of the monomer (**Figure 6**d). Therefore, BSArGO@ZIF-8 NSs showed efficient lethality to cancer cells by causing apoptosis and mitochondrial damage.

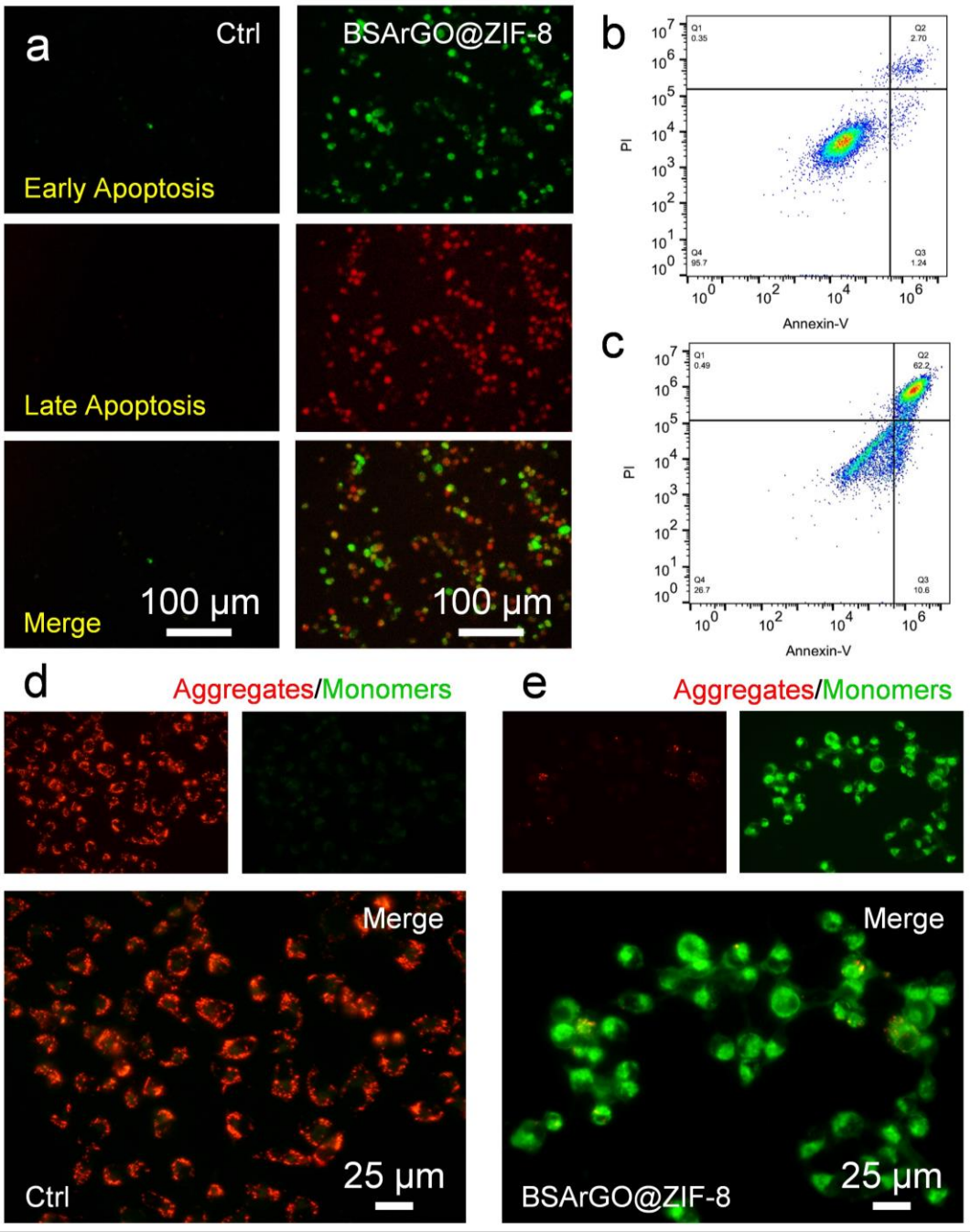

Figure 6. BSArGO@ZIF-8 NSs caused apoptosis and mitochondrial damage of Cal27 cells. a) Fluorescence detection of early and late apoptosis in Cal27 cells treated with BSArGO@ZIF-8 NSs at 150 μg/mL. b, c) Flow cytometry detection of apoptosis effect BSArGO@ZIF-8 NSs at 150 μg/mL on Cal27 cells. d, e) Effect of BSArGO@ZIF-8 NSs on mitochondrial membrane potential changes detected by JC-1.

Synergistic effect of PTT and IIT *in vitro*. To further confirm the synergistic effect of PTT and IIT *in vitro*, the cell viability was measured after NIR irradiation at 808 nm. As shown in **Figure 7**a, BSArGO@ZIF-8 NSs possessed a high cell killing capacity on SCC25 cells (~50%), and the cell viability further decreased to ~15% after NIR irradiation. Similarly, the viability of Cal27 cells was about 50% when treated by BSArGO@ZIF-8 NSs, and decreased to ~20% after irradiation. However, NIR irradiation alone at 808 nm (1 W/cm^{-2}) for 10 min had negligible effects on Cal27 cells (**Figure S22**). Furthermore, the live/dead staining of Cal27 cells was performed. Many dead cells were imaged after BSArGO@ZIF-8 NSs treatment compared with the control group (**Figure 7**c and d). After NIR irradiation, more dead cells emerged and few live cells could be observed (**Figure 7**e). Meanwhile, the dead cell ratios were calculated (**Figure S23**), and were ~14% and ~49% in the BSArGO@ZIF-8 group and the BSArGO@ZIF-8+NIR group, respectively. However, the viability of cells decreased by 56% in the BSArGO@ZIF-8 group, and by 74% in the BSArGO@ZIF-8+NIR group. The difference between the dead cell ratio and cell viability change is likely due to the increased cell number in the control group. Therefore, BSArGO@ZIF-8 NSs are able to mediate the combination of PTT and IIT showing an enhanced lethality to cancer cells. Interestingly, almost all dead cells belonged to late apoptosis and there were almost no early apoptotic cells after NIR irradiation (**Figure 7**f), meaning that PTT can further enhance cell apoptosis.[84] It has been demonstrated that PTT can promote cell apoptosis by inducing lysosome rupture, activating Bid, inducing Bax/Bak oligomerization and pore formation in the mitochondrial outer membrane. As a consequence, cytochrome c would be released, finally leading to apoptosome assembly facilitated by Apaf-1.[85] Therefore, there is a synergistic effect of PTT and Zn-mediated ion interference on cell apoptosis by activating related apoptotic events.

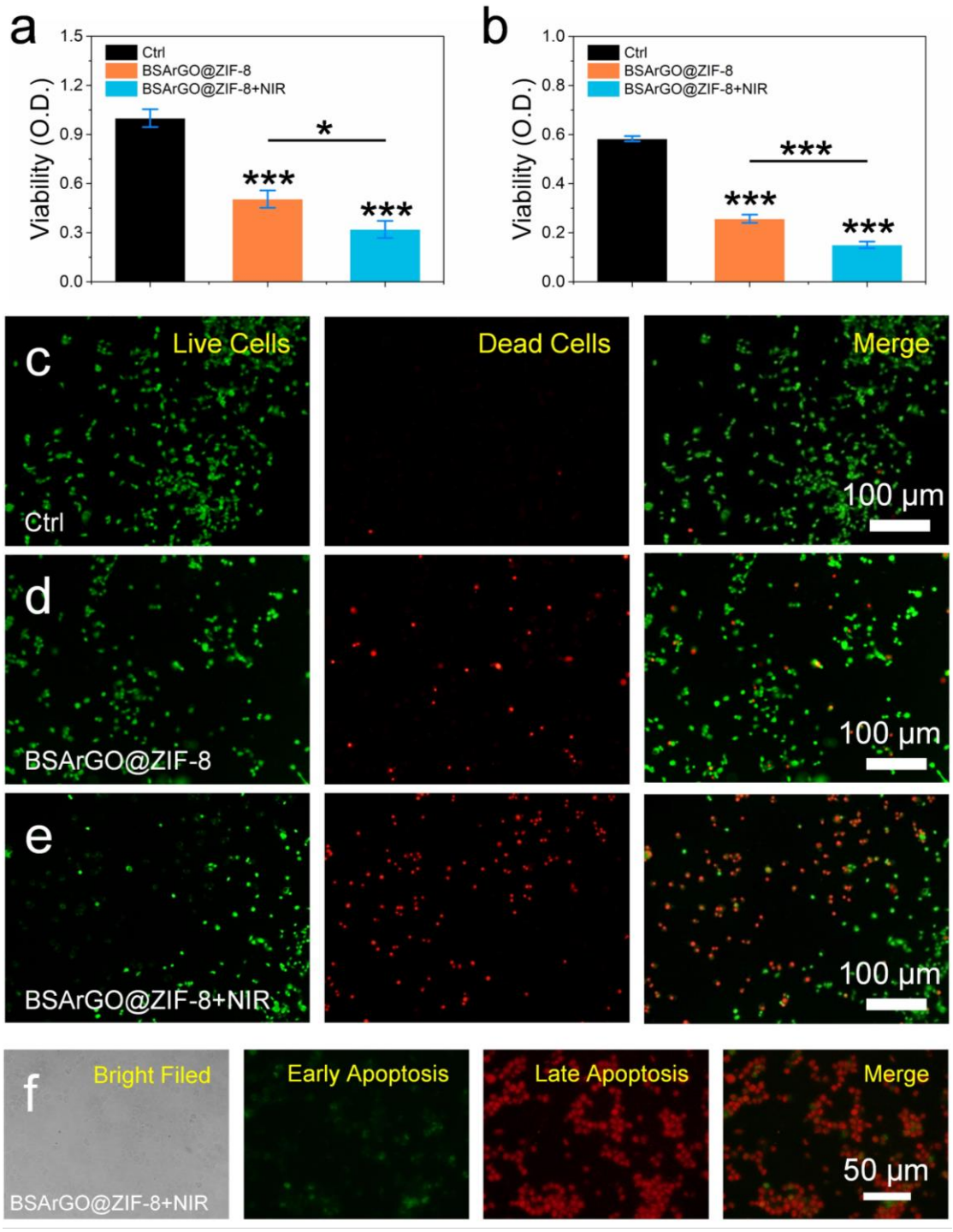

Figure 7. Synergistic effect of PTT and IIT. a, b) Viability of SCC25 cells and Cal27 cells after BSArGO@ZIF-8 NSs treatment with or without NIR irradiation, respectively. (c-e) Live/dead staining of Cal27 cells treated with BSArGO@ZIF-8 NSs with or without NIR irradiation. f) Fluorescence detection of early and late apoptosis in Cal27 cells treated with BSArGO@ZIF-8 NSs and NIR irradiation.

Antitumor efficacy of BSArGO@ZIF-8 NSs *in vivo*. As our system was designed for the treatment of solid tumor, the *in vivo* antitumor efficacy of the BSArGO@ZIF-8 NSs was investigated in BALB/c nude mice bearing Cal27 xenografts. Once the tumor had grown to 400 mm^3, the mice (the number of mice in each group, n = 4) were intratumorally injected with either saline (control) or BSArGO@ZIF-8 NSs (4 mg/mL, 50 μL) every 48 h irradiating or not the tumor. Since NIR irradiation alone had no effect on cancer cells, this group was not set *in vivo*.[86] The intratumoral administration of complex functional nanomaterials is an efficient method to treat solid tumor as being reported in several recent studies.[87-89] A total of 5 injections were performed over 12 days. Notably, after this period, the tumor size visibly decreased in the BSArGO@ZIF-8 NSs group without irradiation compared to the saline group, while NIR irradiation synergistically further decreased the tumor size (**Figure 8**a-c). Meanwhile, BSArGO@ZIF-8 NSs treatment reduced tumor weights (lose mass ratio ~30%) in comparison to those in the saline group, and the weight loss ratio of tumors reached to ~70% after NIR irradiation treatment (**Figure 8**d). These results showed that BSArGO@ZIF-8 NSs already had a certain efficacy of tumor suppression by IIT alone, while BSArGO@ZIF-8 NSs combination of IIT and PTT exhibited a clear inhibition effect enhancement.

According to hematoxylin-eosin (H&E) staining of the tumor tissues, the mice treated with BSArGO@ZIF-8 NSs under NIR irradiation showed many apoptotic cells, whereas a large population of live cancer cells was found in the control group (**Figure 8**e). TdT mediated dUTP nick-end labeling (TUNEL) staining assay confirmed that BSArGO@ZIF-8 NSs can efficiently cause cell apoptosis, and more apoptotic cells appeared after NIR irradiation (**Figure 8**f). In addition, immunohistochemical staining results showed that BSArGO@ZIF-8 NSs significantly decreased the number of Ki67+ and CD31+ cells in the tumor tissues, meaning that cancer cell proliferation and angiogenesis in tumors were both efficiently inhibited (**Figure 8**g-j). The inhibition of proliferation and angiogenesis can further suppress the growth of tumors. The tissue penetration ability of nanomaterials plays an important role in cancer therapy efficacy. To confirm the penetration of these NSs into the tumor after injection, the tumor tissue sections were stained with the Zn^{2+}-detecting probe ZnAF-2 for qualitative characterization of the penetration ability of BSArGO@ZIF-8 NSs. The continuous images taken from the left side to the right side of the tissue section are spliced. According to the result **(Figure S24)**, zinc was distributed in the whole tissue section. Therefore, BSArGO@ZIF-8 NSs have a relatively good penetration ability. Meanwhile, according to the hematological indicators, BSArGO@ZIF-8 NSs

showed no effect on the erythrocyte and platelet markers (**Figure S25**). In addition, histological analyses (H&E staining) of the main organs, including heart, liver, spleen, lung, and kidney, showed BSArGO@ZIF-8 NSs injection with or without NIR irradiation did not induce obvious pathological changes in these organs (**Figure 8**k). Therefore, BSArGO@ZIF-8 NSs combined ion-interference and photothermal therapy displayed low systemic toxicity and high biosecurity, bringing great potential in further clinical applications.

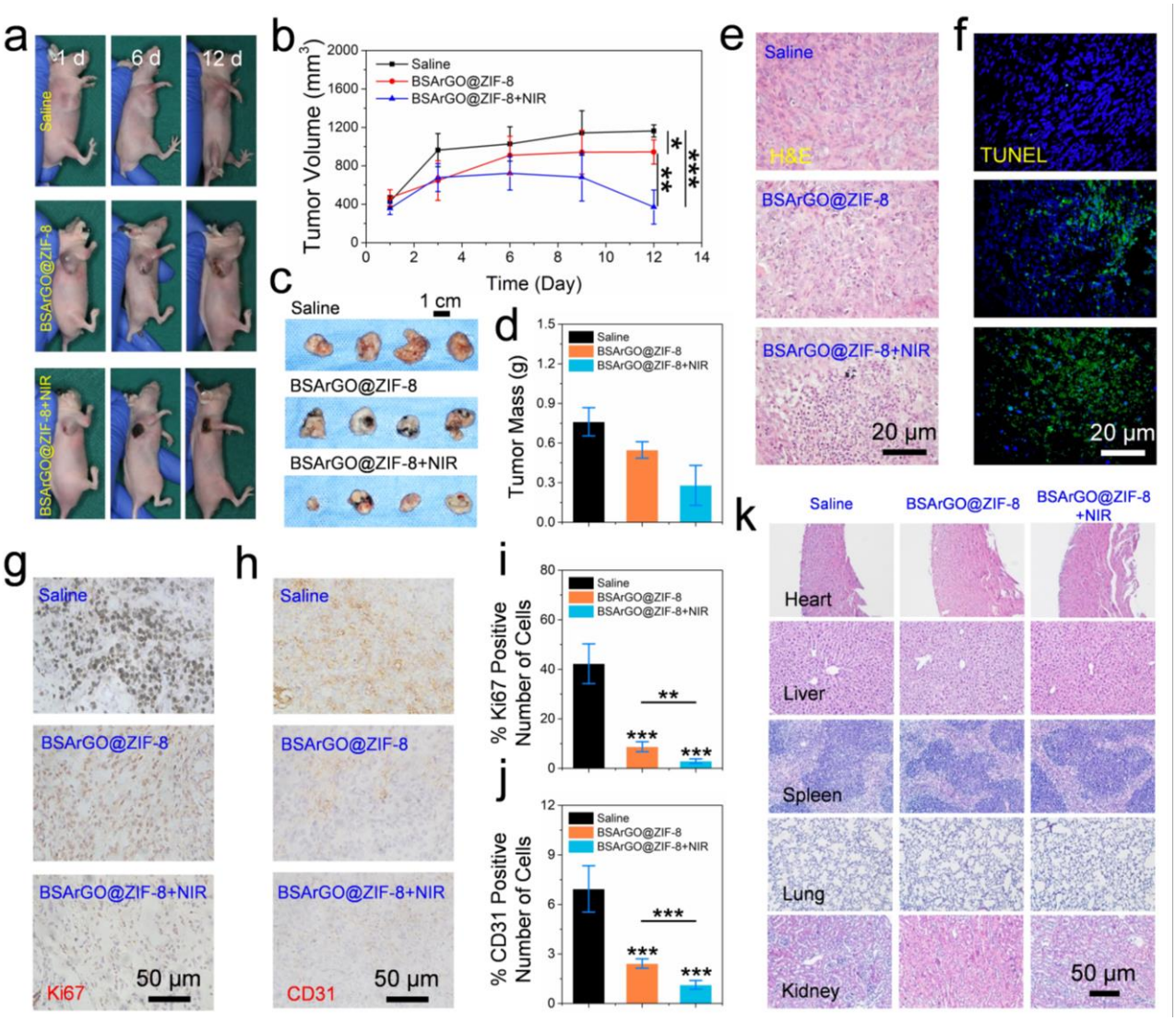

Figure 8. *In vivo* cancer therapeutic efficiency by BSArGO@ZIF-8 NSs mediated ion-interference and photothermal combined therapy in Cal27 orthotopic xenografts on BALB/c nude mice. a) Photos showing the tumor size in mice during BSArGO@ZIF-8 NSs with or without NIR irradiation treatment. b) Tumor size change during therapy. c) Digital pictures of tumors excised from the Cal27 tumor-bearing mice after 12 days of therapy. d) Average tumor mass excised from the Cal27 tumor-bearing mice after treatment. e) H&E staining of tumor sections from the Cal27 tumor-bearing mice. f) TUNEL

staining of tumor sections from the Cal27 tumor-bearing mice. g, h) Immunohistochemistry staining of Ki67 and CD31 in tumor sections. i, j) Statistic analysis of Ki67 and CD31 positive cells in immunohistochemistry staining sections. k) Histological analyses of the major tissues after therapy.

CONCLUSION

In summary, BSArGO@ZIF-8 NSs with relatively high colloidal stability and good dispersibility were prepared by *in situ* growth of ZIF-8 onto the surface of GO, reduction of GO with Vc, and modification with BSA. BSArGO@ZIF-8 NSs caused the intracellular Zn^{2+} overload and ROS increase, and showed a broad-spectrum high lethality to different types of cancer cells. BSArGO@ZIF-8 NSs could initiate bim-mediated mitochondrial apoptotic events and change the pro-apoptotic gene expression to synergistically promote cell apoptosis. Meanwhile, the overloaded intracellular Zn^{2+} triggered cellular dysfunctions and mitochondria damage by activating the autophagy signaling pathways and influencing the intracellular environmental homeostasis. Combined with the photothermal effect of rGO, BSArGO@ZIF-8 NSs possessed higher killing capacity to cancer cells under NIR irradiation. Compared with BSArGO@ZIF-8 NSs alone, BSArGO@ZIF-8 NSs-mediated ion-interference and photothermal combined therapy caused apoptosis and inhibited cell proliferation and angiogenesis more effectively, bringing a satisfactory efficacy to suppress tumor growth *in vivo*. Furthermore, BSArGO@ZIF-8 NSs showed low systemic toxicity with or without NIR irradiation. Therefore, the designed Zn-based multifunctional nanoplatforms will allow promoting the development of IIT and the corresponding combined cancer therapy strategies. Our current work has demonstrated the applicability of ZIF-8 mediated ion interference therapy by triggering an increase in ROS level, mitochondrial damage and apoptosis. In comparison to a previous study,[13] we have elucidated in more detail the mechanisms of zinc-mediated intracellular interference processes. The conclusions drawn from our results will remind that the Zn^{2+}-interference effect should be considered in the therapeutic efficacy assessment of Zn^{2+}-containing nanocomposites, especially when Zn^{2+}-based nanomaterials are used as drug carriers. We would like to underline that the design of multifunctional nanoparticles is in line with other recent studies where different types of complex nanosystems have been explored for intratumoral anticancer therapies.[87-91] Finally, ZIF-8 core-shell nanostructures with smaller size

coated with GQDs or polydopamine will be designed to broaden cancer therapy modalities (e.g., exploiting intravenous injection).

EXPERIMENTAL SECTION

BSArGO@ZIF-8 NSs synthesis. Two mL of 2-MIM (2-methylimidazole) (203 mg) methanol solution and 1.2 mL of $Zn(NO_3)_2 \cdot 6H_2O$ (92 mg) methanol solution were mixed under stirring. Then, 0.8 mL 1 mg/mL GO was slowly added into the mixture. After 1 h, 1 mL of 5 mg/mL Vc was slowly added and stirred for another 3 h to form rGO@ZIF-8 NSs. The mixture solution was centrifuged at 8000 rpm for 5 min, and the precipitate was washed with the methanol to remove the excess Vc. Finally, the precipitate was dispersed in 2 mL methanol and 8 mL of 4 mg/mL BSA were added, and then stirred for 30 min. After this reaction, the precipitate was collected by centrifugation (8000 rpm for 5 min) and subsequently washed with water. Finally, the prepared BSArGO@ZIF-8 NSs were dispersed in water and stored at 4 ℃ for the following experiments.

Characterization of BSArGO@ZIF-8 NSs. The morphology of rGO@ZIF-8 NSs and BSArGO@ZIF-8 NSs was observed by a transmission electron microscope (TEM, Hitachi 7500, Hitachi High Technologies Corporation, Tokyo, Japan). The size of ZIF-8 NPs was measured by ImageJ. XRD patterns of BSArGO@ZIF-8 NSs were recorded on a Bruker D8 advance powder diffractometer (Cu Kα X-ray source). XPS spectra were measured by a Thermo Scientific K-Alpha X-ray photoelectron spectrometer with a basic chamber pressure of 10^{-8} to 10^{-9} bar with an anode using Al Kα radiation ($h\nu$ = 1486.6 eV). Raman spectra were obtained by a Renishaw inVia microscope equipped with a 532 nm laser.

Cell culture and cell viability. Human cervical carcinoma (HeLa) cells and human head and neck squamous cell carcinoma (SCC25, Cal27, and HN4) cells were obtained from ATCC (ATCC, Manassas, VA, USA). Cells were cultured in a DMEM medium (Hyclone, Logan, UT, USA) supplemented with 10% fetal bovine serum. Cell viability was detected by a cell counting kit-8 (CCK-8, Dojindo Molecular Technology) test following the manufacturer's instructions.

Live/dead cell staining assay. SCC25 and Cal27 cells were cultured in DMEM containing 200 μg/mL and 150 μg/mL BSArGO@ZIF-8 NSs respectively for 24 h in 24-well plates using the live/dead cell double staining kit (Solarbio, Beijing, China). After incubation at 37 ℃ for 20 min in the dark, the cells were washed with PBS and observed under an Olympus IX73 inverted fluorescence Microscope.

Intracellular ROS and Zn^{2+} detection assay. After co-culturing with BSArGO@ZIF-8 NSs for 6 h, intracellular ROS level was measured using 2′,7′-dichlorofluorescein diacetate (Beyotime Biotechnology, Shanghai, China) for 20 min and washed three times with PBS. Intracellular Zn^{2+} level was measured by Zn^{2+} probe (Abcam, Cambridge, UK). Untreated cells were used as control. The ROS signal and Zn^{2+} level in the cells were observed by inverted fluorescence microscopy and ImageJ software was used for semi-quantitative analysis. In addition, the intracellular ROS and Zn^{2+} ion level in SCC25, Cal27, and HeLa cells with or without BSArGO@ZIF-8 NSs treatment were detected by flow cytometry (BD Biosciences, San Diego, CA, USA).

RNA-seq analysis. Total RNA of Cal27 cells from 3 different experiments treated with or without BSArGO@ZIF-8 NSs for 6 h was collected and RNA-seq was used to analyze the whole genome expression at LC Sciences through the Illumina X10 platform (Hangzhou, Zhejiang, China). Firstly, the total RNA was performed quality control based on the previous study, and then the clean reads were mapped to the reference genome (GRCh38) via hierarchical indexing for spliced alignment of transcripts (HISAT) (v2.0.4). StringTie was used to determine the expression level of mRNAs by calculating fragments per kilobase of exon model per million mapped fragments (FPKM). The correlation among all samples was detected by Pearson correlation analysis and PCA. Volcano analysis was used to identify the DEGs between the treated and control groups. Based on the DEGs generated by BSArGO@ZIF-8 NSs, the overrepresented Gene Ontology categories and the significant KEGG pathways were identified. Heatmaps were used to present the expression signatures of the DEGs involved in cell apoptosis and cancer-related pathways. The Pathview website was used to analyze the signaling pathway activation after BSArGO@ZIF-8 NSs treatment. To select the genes that were not significantly differentially expressed but were important for the function of biological pathways, GSEA was performed method according to all genes in BSArGO@ZIF-8 NSs vs control group based on the cluster Profiler and enrichplot R package. The RNA sequence data are available at the NCBI Gene Expression Omnibus (GEO): GSE191172.

Mitochondrial membrane potential and cell apoptosis analysis. To detect the variations of mitochondrial membrane potential, Cal27 cells were treated with 150 μg/mL BSArGO@ZIF-8 NSs for 6 h. Untreated cells were as control. Then, cells were washed with PBS and labeled with JC-1 (5,5′,6,6′-tetrachloro-1,1′,3,3′-tetraethyl benzimidazolylcarbocyanine iodide; Solarbio) at 37°C in the dark for 30 min. Labeled cells were washed twice with PBS and observed by fluorescence microscopy.

The state of Cal27 apoptosis after BSArGO@ZIF-8 NSs treatment for 12 h was measured. Untreated cells were used as control. According to the manufacturer's instructions, the cells were harvested and processed for apoptosis analysis by Annexin V-FITC/PI staining (Dojindo Laboratories). The early and late apoptosis signals were observed by fluorescence microscopy and measured by cytometry analysis.

Synergistic effect of PTT and IIT *in vitro*. After treatment with BSArGO@ZIF-8 NSs for 12 h at the concentration of 150 μg/mL (Cal27 cells) and 200 μg/mL (SCC25 cells), 808 nm NIR irradiation (1W/cm^2) was performed for 10 min. After being cultured for an additional 12 h, cell viability and live/dead cell staining were performed.

Animal experiments. For *in vivo* assays, 12 female BALB/c nude mice (5 weeks of age) were purchased from Beijing Vital River Laboratory Animal Technology Co., Ltd. (Beijing, China). Experimental protocols were conducted according to ethical principles for using laboratory animals, as approved by the Medical Ethics Committee of the School of Stomatology, Shandong University, Jinan, China (protocol: 20210304). After a week of acclimatization, the mice were injected with Cal27 cells (4×10^6 cells in 200 μL saline) under the right axilla. Tumor volume (V) was calculated by tumor length (L) and width (W) as $V = L \times W^2 / 2$. When the tumor volume reached 400 mm^3, the mice were randomly divided into three groups, with four repeats for each group: (i) saline, (ii) BSArGO@ZIF-8, (iii) BSArGO@ZIF-8+NIR. BSArGO@ZIF-8 NSs (4 mg/mL, 50 μL) dispersion were injected intratumorally every other day. Additionally, group (iii) was treated with the 808 nm laser for 10 min at 1 W/cm^2 after 24 h post-injection. Meanwhile, the mice were photographed, the changes in weight and the tumor volume of mice in each group were recorded. After 12 days, about 200 μL of blood was collected for hematological analysis and all the mice were sacrificed by cervical dislocation. The tumors were excised, weighed, photographed, and stored for further investigation. The major organs (heart, liver, spleen, lung, and kidney) were also collected. After they were fixed with 4% paraformaldehyde, dehydrated, sliced, and stained with H&E or immunohistochemical staining using Ki67 and CD31 (Abcam). For apoptosis analysis of the cancer cells, terminal deoxynucleotidyl transferase-mediated dUTP nick-end labeling (TUNEL) staining analysis was performed on the tumor sections. The slices were imaged by fluorescence microscopy. To further confirm the penetration, tumor tissue sections were stained for 2 h at room temperature with 20 μM of fluorophore ZnAF-2F.

The continuous images taken using a fluorescent microscope along the approximately 4 mm long tissue piece from the left side to the right side are spliced.

Statistical analysis. The results are shown as the mean ± standard deviation of the mean. The statistical significance of the differences was determined by one-way ANOVA. Values with $p < 0.05$ were considered statistically significant in the biological experiment (*means $p < 0.05$, ** means $p < 0.01$, *** means $p < 0.001$). In the process of RNA-seq analysis, q (the corrected p value, FDR) < 0.05 was considered to detect DEGs.

ASSOCIATED CONTENT

Supporting Information

The Supporting Information is available free of charge on the ACS Publications website at https://pubs.acs.org/doi/

Figures S1−S25 (PDF): Data of the color of rGO@ZIF-8, XRD pattern of rGO@ZIF-8 NSs, FT-IR spectra of rGO@ZIF-8 and BSArGO@ZIF-8 NSs, the stability of BSArGO@ZIF-8 NSs in PBS, the size distribution of BSArGO@ZIF-8 NSs, morphology of BSAZIF-8 without GO as *in situ* growth template, ultraviolet absorbance spectra of BSArGO@ZIF-8 NSs at different concentrations, temperature curves of BSArGO@ZIF-8 NSs at different concentrations under NIR irradiation, Zn^{2+} release ratio after dispersed in PBS at different pH, toxicity of GO on Cal27 cells, toxicity of rGO on Cal27 cells, toxicity of BSAZIF-8 on Cal27 cells, toxicity of BSArGO@ZIF-8 NSs, intracellular Zn^{2+} content and ROS level change in HeLa cells after BSArGO@ZIF-8 NSs treatment, lysosome colocalization, PCA analysis and DEGs statistics in Cal27 cells with or without BSArGO@ZIF-8 NSs treatment, GO enrichment analysis of DEGs in BSArGO@ZIF-8 NSs intracellular delivery, DEGs in specific pathways, Pathview analysis of autophagy signaling pathway and cancer signaling pathway based on KEGG database in Cal27 cells after BSArGO@ZIF-8 NSs treatment, cellular response to Zn^{2+} signaling pathways based on GSEA, heatmap of cellular response to Zn^{2+} associated DEGs, cell cycle signaling pathways based on GSEA, heatmap of cell cycle associated DEGs, viability of Cal27 cells after sole NIR irradiation treatment, the ratio of dead Cal27 cells after the different treatments, tumor tissue section staining of Zn^{2+} and whole blood cell analysis of BALB/c nude mice undergoing Cal27 orthotopic xenografts and following BSArGO@ZIF-8 NSs (with or without NIR irradiation) treatment.

Author Contributions

[#]C. L. and W. K. contributed equally.

Notes

The authors declare no competing financial interest.

ORCID

Yuta Nishina: 0000-0002-4958-1753

Shaohua Ge: 0000-0003-3821-5480

Alberto Bianco: 0000-0002-1090-296X

Baojin Ma: 0000-0001-5545-5078

ACKNOWLEDGMENTS

The authors greatly acknowledge the financial support from the National Natural Science Foundation of China (No. 82100974, 82170964, and 82101020), The Major Innovation Projects in Shandong Province (No. 2021SFGC0502), The Construction Engineering Special Fund of "Taishan Scholars" of Shandong Province (No.ts20190975 and tsqn201909180), Collaborative Innovation Center of Technology and Equipment for Biological Diagnosis and Therapy in Universities of Shandong, Shandong Province Natural Science Foundation (ZR2021QH241 and ZR202102180927), Qilu Young Scholars Program of Shandong University. This work was partly supported by the Agence Nationale de la Recherche (ANR) through the LabEx project Chemistry of Complex Systems (ANR-10-LABX-0026_CSC). We wish to also acknowledge the Centre National de la Recherche Scientifique (CNRS), the International Center for Frontier Research in Chemistry (icFRC). We also acknowledge CNRS through the international research project "MULTIDIM" between UPR3572 and Okayama University.

REFERENCES

(1) López-Hernández, T.; Puchkov, D.; Krause, E.; Maritzen, T.; Haucke, V. Endocytic Regulation of Cellular Ion Homeostasis Controls Lysosome Biogenesis. *Nat. Cell Biol.* **2020,** *22*, 815−827.

(2) Banerjee, I.; Behl, B.; Mendonca, M.; Shrivastava, G.; Russo, A. J.; Menoret, A.; Ghosh, A.; Vella,

A. T.; Vanaja, S. K.; Sarkar, S. N.; Fitzgerald, K. A.; Rathinam, V. A. K. Gasdermin D Restrains Type I Interferon Response to Cytosolic DNA by Disrupting Ionic Homeostasis. *Immunity* **2018,** *49*, 413−426.e5.

(3) Autzen, H. E.; Myasnikov, A. G.; Campbell, M. G.; Asarnow, D.; Julius, D.; Cheng, Y. Structure of the Human Trpm4 Ion Channel in a Lipid Nanodisc. *Science* **2018,** *359*, 228−232.

(4) Giorgi, C.; Marchi, S.; Pinton, P. The Machineries, Regulation and Cellular Functions of Mitochondrial Calcium. *Nat. Rev. Mol. Cell Biol.* **2018,** *19*, 713−730.

(5) Puig, S.; Askeland, E.; Thiele, D. J. Coordinated Remodeling of Cellular Metabolism During Iron Deficiency through Targeted Mrna Degradation. *Cell* **2005,** *120*, 99−110.

(6) Wang, Q. C.; Zheng, Q.; Tan, H.; Zhang, B.; Li, X.; Yang, Y.; Yu, J.; Liu, Y.; Chai, H.; Wang, X.; Sun, Z.; Wang, J. Q.; Zhu, S.; Wang, F.; Yang, M.; Guo, C.; Wang, H.; Zheng, Q.; Li, Y.; Chen, Q.; Zhou, A.; Tang, T. S. Tmco1 Is an Er Ca^{2+} Load-Activated Ca^{2+} Channel. *Cell* **2016,** *165*, 1454−1466.

(7) McCord, M. C.; Aizenman, E. Convergent Ca^{2+} and Zn^{2+} Signaling Regulates Apoptotic Kv2.1 K^{+} Currents. *Proc. Natl. Acad. Sci. USA* **2013,** *110*, 13988−13993.

(8) Deng, H.; Qiao, X.; Xie, T.; Fu, W.; Li, H.; Zhao, Y.; Guo, M.; Feng, Y.; Chen, L.; Zhao, Y.; Miao, L.; Chen, C.; Shen, K.; Wang, X. SLC-30A9 Is Required for Zn^{2+} Homeostasis, Zn^{2+} Mobilization, and Mitochondrial Health. *Proc. Natl. Acad. Sci. USA* **2021,** *118*, e2023909118.

(9) Liu, Y.; Zhang, M.; Bu, W. Bioactive Nanomaterials for Ion-Interference Therapy. *VIEW* **2020,** *1*, e18.

(10) Chi, Y.; Sun, P.; Gao, Y.; Zhang, J.; Wang, L. Ion Interference Therapy of Tumors Based on Inorganic Nanoparticles. *Biosensors* **2022,** *12*, 100.

(11) Liu, B.; Bian, Y.; Liang, S.; Yuan, M.; Dong, S.; He, F.; Gai, S.; Yang, P.; Cheng, Z.; Lin, J. One-Step Integration of Tumor Microenvironment-Responsive Calcium and Copper Peroxides Nanocomposite for Enhanced Chemodynamic/Ion-Interference Therapy. *ACS Nano* **2022,** *16*, 617−630.

(12) Gong, F.; Xu, J.; Liu, B.; Yang, N.; Cheng, L.; Huang, P.; Wang, C.; Chen, Q.; Ni, C.; Liu, Z. Nanoscale CaH_2 Materials for Synergistic Hydrogen-Immune Cancer Therapy. *Chem* **2022,** *8*, 268−286.

(13) Wu, S.; Zhang, K.; Liang, Y.; Wei, Y.; An, J.; Wang, Y.; Yang, J.; Zhang, H.; Zhang, Z.; Liu, J. Nano-Enabled Tumor Systematic Energy Exhaustion Via Zinc (II) Interference Mediated Glycolysis

Inhibition and Specific GLUT1 Depletion. *Adv. Sci.* **2022,** *9*, 2103534.

(14) Ding, X.-L.; Liu, M.-D.; Cheng, Q.; Guo, W.-H.; Niu, M.-T.; Huang, Q.-X.; Zeng, X.; Zhang, X.-Z. Multifunctional Liquid Metal-Based Nanoparticles with Glycolysis and Mitochondrial Metabolism Inhibition for Tumor Photothermal Therapy. *Biomaterials* **2022**, 121369.

(15) Zhao, H.; Wang, L.; Zeng, K.; Li, J.; Chen, W.; Liu, Y.-N. Nanomessenger-Mediated Signaling Cascade for Antitumor Immunotherapy. *ACS Nano* **2021,** *15*, 13188−13199.

(16) Dalisson, B.; Barralet, J. Bioinorganics and Wound Healing. *Adv. Healthc. Mater.* **2019,** *8*, e1900764.

(17) Wang, X.; Li, Y.; Deng, X.; Jia, F.; Cui, X.; Lu, J.; Pan, Z.; Wu, Y. Colloidally Stabilized Dspe-Peg-Glucose/Calcium Phosphate Hybrid Nanocomposites for Enhanced Photodynamic Cancer Therapy Via Complementary Mitochondrial Ca^{2+} Overload and Autophagy Inhibition. *ACS Appl. Mater. Interfaces* **2021,** *13*, 39112−39125.

(18) Zheng, P.; Ding, B.; Jiang, Z.; Xu, W.; Li, G.; Ding, J.; Chen, X. Ultrasound-Augmented Mitochondrial Calcium Ion Overload by Calcium Nanomodulator to Induce Immunogenic Cell Death. *Nano Lett.* **2021,** *21*, 2088−2093.

(19) Zhang, M.; Song, R.; Liu, Y.; Yi, Z.; Bu, W. Calcium-Overload-Mediated Tumor Therapy by Calcium Peroxide Nanoparticles. *Chem* **2019,** *5*, 2171−2182.

(20) Li, Y.; Zhou, S.; Song, H.; Yu, T.; Zheng, X.; Chu, Q. Caco(3) Nanoparticles Incorporated with KAE to Enable Amplified Calcium Overload Cancer Therapy. *Biomaterials* **2021,** *277*, 121080.

(21) Jiang, W.; Yin, L.; Chen, H.; Paschall, A. V.; Zhang, L.; Fu, W.; Zhang, W.; Todd, T.; Yu, K. S.; Zhou, S.; Zhen, Z.; Butler, M.; Yao, L.; Zhang, F.; Shen, Y.; Li, Z.; Yin, A.; Yin, H.; Wang, X.; Avci, F. Y.; Yu, X.; Xie, J. Nacl Nanoparticles as a Cancer Therapeutic. *Adv. Mater.* **2019,** *31*, 1904058.

(22) Chai, Q.; Xie, L.; Gao, M.; Liu, Y.; Xu, X.; Huang, X.; Chen, P.; Wu, T.; Wan, Q.; Kong, B. Super-Assembled Silica Nanoprobes for Intracellular Zn(II) Sensing and Reperfusion Injury Treatment through in Situ Mof Crystallization. *Analyst* **2021,** *146*, 6788−6797.

(23) Corkins, M. E.; May, M.; Ehrensberger, K. M.; Hu, Y. M.; Liu, Y. H.; Bloor, S. D.; Jenkins, B.; Runge, K. W.; Bird, A. J. Zinc Finger Protein Loz1 Is Required for Zinc-Responsive Regulation of Gene Expression in Fission Yeast. *Proc. Natl. Acad. Sci. USA* **2013,** *110*, 15371−15376.

(24) Kim, S. W.; Lee, H. K.; Kim, H. J.; Yoon, S. H.; Lee, J. K. Neuroprotective Effect of Ethyl Pyruvate against Zn^{2+} Toxicity Via Nad Replenishment and Direct Zn^{2+} Chelation.

Neuropharmacology **2016,** *105*, 411−419.

(25) Fuselli, S.; De Felice, M.; Morlino, R.; Turrio-Baldassarri, L. Correction: Fuselli, Et Al. A Three Year Study on 14 Vocs at One Site in Rome: Levels, Seasonal Variations, Indoor / Outdoor Ratio and Temporal Trends. *Int. J. Environ. Res. Public Health* **2010,** *7*2, 3792−3803.

(26) Haase, H.; Wätjen, W.; Beyersmann, D. Zinc Induces Apoptosis That Can Be Suppressed by Lanthanum in C6 Rat Glioma Cells. *Biol. Chem.* **2001,** *382*, 1227−1234.

(27) Li, S.; Wang, K.; Shi, Y.; Cui, Y.; Chen, B.; He, B.; Dai, W.; Zhang, H.; Wang, X.; Zhong, C.; Wu, H.; Yang, Q.; Zhang, Q. Novel Biological Functions of ZIF-NP as a Delivery Vehicle: High Pulmonary Accumulation, Favorable Biocompatibility, and Improved Therapeutic Outcome. *Adv. Funct. Mater.* **2016,** *26*, 2715−2727.

(28) Zheng, H.; Zhang, Y.; Liu, L.; Wan, W.; Guo, P.; Nyström, A. M.; Zou, X. One-Pot Synthesis of Metal–Organic Frameworks with Encapsulated Target Molecules and Their Applications for Controlled Drug Delivery. *J. Am. Chem. Soc.* **2016,** *138*, 962−968.

(29) Wang, Q.; Sun, Y.; Li, S.; Zhang, P.; Yao, Q. Synthesis and Modification of Zif-8 and Its Application in Drug Delivery and Tumor Therapy. *RSC Adv.* **2020,** *10*, 37600−37620.

(30) Li, Y.; Gong, T.; Gao, H.; Chen, Y.; Li, H.; Zhao, P.; Jiang, Y.; Wang, K.; Wu, Y.; Zheng, X. ZIF-Based Nanoparticles Combine X-Ray-Induced Nitrosative Stress with Autophagy Management for Hypoxic Prostate Cancer Therapy. *Angew. Chem. Int. Ed.* **2021,** *60*, 15472−15481.

(31) Zhao, H.; Li, T.; Yao, C.; Gu, Z.; Liu, C.; Li, J.; Yang, D. Dual Roles of Metal-Organic Frameworks as Nanocarriers for Mirna Delivery and Adjuvants for Chemodynamic Therapy. *ACS Appl. Mater. Interfaces* **2021,** *13*, 6034−6042.

(32) Wu, Q.; Li, M.; Tan, L.; Yu, J.; Chen, Z.; Su, L.; Ren, X.; Fu, C.; Ren, J.; Li, L.; Cao, F.; Liang, P.; Zhang, Y.; Meng, X. A Tumor Treatment Strategy Based on Biodegradable BSA@ZIF-8 for Simultaneously Ablating Tumors and Inhibiting Infection. *Nanoscale Horiz.* **2018,** *3*, 606−615.

(33) Shi, L.; Wu, J.; Qiao, X.; Ha, Y.; Li, Y.; Peng, C.; Wu, R. In Situ Biomimetic Mineralization on Zif-8 for Smart Drug Delivery. *ACS Biomater. Sci. Eng.* **2020,** *6*, 4595−4603.

(34) Martín, C.; Ruiz, A.; Keshavan, S.; Reina, G.; Murera, D.; Nishina, Y.; Fadeel, B.; Bianco, A. A Biodegradable Multifunctional Graphene Oxide Platform for Targeted Cancer Therapy. *Adv. Funct. Mater.* **2019,** *29*, 1901761.

(35) Qin, Y.; Li, J.; Kong, Y.; Li, X.; Tao, Y.; Li, S.; Wang, Y. In Situ Growth of Au Nanocrystals on

Graphene Oxide Sheets. *Nanoscale* **2014,** *6*, 1281−1285.

(36) Zhang, J.; Li, Z.; Qi, X.; Zhang, W.; Wang, D.-Y. Size Tailored Bimetallic Metal-Organic Framework (Mof) on Graphene Oxide with Sandwich-Like Structure as Functional Nano-Hybrids for Improving Fire Safety of Epoxy. *Compos. Part B-Eng.* **2020,** *188*, 107881.

(37) Kurapati, R.; Mukherjee, S. P.; Martín, C.; Bepete, G.; Vázquez, E.; Pénicaud, A.; Fadeel, B.; Bianco, A. Degradation of Single-Layer and Few-Layer Graphene by Neutrophil Myeloperoxidase. *Angew. Chem. Int. Ed.* **2018,** *57*, 11722−11727.

(38) Lima-Sousa, R.; de Melo-Diogo, D.; Alves, C. G.; Costa, E. C.; Ferreira, P.; Louro, R. O.; Correia, I. J. Hyaluronic Acid Functionalized Green Reduced Graphene Oxide for Targeted Cancer Photothermal Therapy. *Carbohydr. Polym.* **2018,** *200*, 93−99.

(39) Zhang, H.; Wu, H.; Wang, J.; Yang, Y.; Wu, D.; Zhang, Y.; Zhang, Y.; Zhou, Z.; Yang, S. Graphene Oxide-Bagdf5 Nanocomposites for Multi-Modal Imaging and Photothermal Therapy. *Biomaterials* **2015,** *42*, 66−77.

(40) An, D.; Fu, J.; Zhang, B.; Xie, N.; Nie, G.; Ågren, H.; Qiu, M.; Zhang, H. NIR-II Responsive Inorganic 2D Nanomaterials for Cancer Photothermal Therapy: Recent Advances and Future Challenges. *Adv. Funct. Mater.* **2021,** *31*, 2101625.

(41) Ma, B.; Bianco, A. Recent Advances in 2D Material‐Mediated Immuno-Combined Cancer Therapy. *Small* **2021,** *17*, 2102557.

(42) Wang, Y.; Meng, H.-M.; Li, Z. Near-Infrared Inorganic Nanomaterial-Based Nanosystems for Photothermal Therapy. *Nanoscale* **2021,** *13*, 8751−8772.

(43) Gu, Z.; Zhu, S.; Yan, L.; Zhao, F.; Zhao, Y. Graphene-Based Smart Platforms for Combined Cancer Therapy. *Adv. Mater.* **2019,** *31*, 1800662.

(44) Ma, B.; Martín, C.; Kurapati, R.; Bianco, A. Degradation-by-Design: How Chemical Functionalization Enhances the Biodegradability and Safety of 2d Materials. *Chem. Soc. Rev.* **2020,** *49*, 6224−6247.

(45) Tian, Z.; Yao, X.; Ma, K.; Niu, X.; Grothe, J.; Xu, Q.; Liu, L.; Kaskel, S.; Zhu, Y. Metal-Organic Framework/Graphene Quantum Dot Nanoparticles Used for Synergistic Chemo-and Photothermal Therapy. *ACS Omega* **2017,** *2*, 1249−1258.

(46) Ma, B.; Nishina, Y.; Bianco, A. A Glutathione Responsive Nanoplatform Made of Reduced Graphene Oxide and Mno2 Nanoparticles for Photothermal and Chemodynamic Combined Therapy.

Carbon **2021,** *178*, 783−791.

(47) Ilhan, B.; Guneri, P.; Wilder-Smith, P. The Contribution of Artificial Intelligence to Reducing the Diagnostic Delay in Oral Cancer. *Oral Oncology* **2021,** *116*, 105254.

(48) Wang, Z.; Wu, V. H.; Allevato, M. M.; Gilardi, M.; He, Y.; Luis Callejas-Valera, J.; Vitale-Cross, L.; Martin, D.; Amornphimoltham, P.; Mcdermott, J. Syngeneic Animal Models of Tobacco-Associated Oral Cancer Reveal the Activity of in Situ Anti-Ctla-4. *Nat. Commun.* **2019,** *10*, 1−13.

(49) Wei, J.; Hu, Y.; Liang, Y.; Kong, B.; Zheng, Z.; Zhang, J.; Zhao, Y.; Wang, H. Graphene Oxide/Core–Shell Structured Metal–Organic Framework Nano-Sandwiches and Their Derived Cobalt/N-Doped Carbon Nanosheets for Oxygen Reduction Reactions. *J. Mater. Chem. A* **2017,** *5*, 10182−10189.

(50) Ma, B.; Guo, S.; Nishina, Y.; Bianco, A. Reaction between Graphene Oxide and Intracellular Glutathione Affects Cell Viability and Proliferation. *ACS Appl. Mater. Interfaces* **2021,** *13*, 3528-3535.

(51) Zhang, J.; Yang, H.; Shen, G.; Cheng, P.; Zhang, J.; Guo, S. Reduction of Graphene Oxide Via L-Ascorbic Acid. *Chem. Commun.* **2010,** *46*, 1112−1114.

(52) Zhang, Y.; Park, S.-J. Stabilization of Dispersed Cupd Bimetallic Alloy Nanoparticles on ZIF-8 for Photoreduction of Cr(VI) in Aqueous Solution. *Chem. Eng. J.* **2019,** *369*, 353−362.

(53) Zhao, S.; Gao, Y.; Tan, J.; Zhu, Y.; Ying, X.; Zhang, M.; Yu, X.; You, B. Facile Synthesis and Antibacterial Applications of Cuprous Oxide/Bovine Serum Albumin Hierarchical Nanocomposite Particles. *SN Appl. Sci.* **2019,** *1*, 917.

(54) Lu, X. F.; Yu, L.; Zhang, J.; Lou, X. W. Ultrafine Dual-Phased Carbide Nanocrystals Confined in Porous Nitrogen-Doped Carbon Dodecahedrons for Efficient Hydrogen Evolution Reaction. *Adv. Mater.* **2019,** *31*, 1900699.

(55) Wu, Q.; Li, M.; Tan, L.; Yu, J.; Chen, Z.; Su, L.; Ren, X.; Fu, C.; Ren, J.; Li, L. A Tumor Treatment Strategy Based on Biodegradable BSA@ZIF-8 for Simultaneously Ablating Tumors and Inhibiting Infection. *Nanoscale Horiz.* **2018,** *3*, 606−615.

(56) Wang, J.; Gao, L.; Zhao, J.; Zheng, J.; Wang, J.; Huang, J. A Facile in–Situ Synthesis of ZIF-8 Nanoparticles Anchored on Reduced Graphene Oxide as a Sulfur Host for Li-S Batteries. *Mater. Res. Bull.* **2021,** *133*, 111061.

(57) Bonakala, S.; Lalitha, A.; Shin, J. E.; Moghadam, F.; Semino, R.; Park, H. B.; Maurin, G. Understanding of the Graphene Oxide/Metal-Organic Framework Interface at the Atomistic Scale.

ACS Appl. Mater. Interfaces **2018,** *10*, 33619−33629.

(58) Martindale, B. C.; Joliat, E.; Bachmann, C.; Alberto, R.; Reisner, E. Clean Donor Oxidation Enhances the H_2 Evolution Activity of a Carbon Quantum Dot-Molecular Catalyst Photosystem. *Angew. Chem. Int. Ed.* **2016,** *55*, 9402−9406.

(59) Yuan, X.; Qu, S.; Huang, X.; Xue, X.; Yuan, C.; Wang, S.; Wei, L.; Cai, P. Design of Core-Shelled g-C3N4@ZIF-8 Photocatalyst with Enhanced Tetracycline Adsorption for Boosting Photocatalytic Degradation. *Chem. Eng. J.* **2021,** *416*, 129148.

(60) Li, S.; Deng, Q.; Zhang, Y.; Li, X.; Wen, G.; Cui, X.; Wan, Y.; Huang, Y.; Chen, J.; Liu, Z. Rational Design of Conjugated Small Molecules for Superior Photothermal Theranostics in the NIR-II Biowindow. *Adv. Mater.* **2020,** *32*, 2001146.

(61) Guo, Z.; Lu, J.; Wang, D.; Xie, W.; Chi, Y.; Xu, J.; Takuya, N.; Zhang, J.; Xu, W.; Gao, F.; Wu, H.; Zhao, L. Galvanic Replacement Reaction for in Situ Fabrication of Litchi-Shaped Heterogeneous Liquid Metal-Au Nano-Composite for Radio-Photothermal Cancer Therapy. *Bioact. Mater.* **2021,** *6*, 602−612.

(62) Bozym, R. A.; Chimienti, F.; Giblin, L. J.; Gross, G. W.; Korichneva, I.; Li, Y.; Libert, S.; Maret, W.; Parviz, M.; Frederickson, C. J.; Thompson, R. B. Free Zinc Ions Outside a Narrow Concentration Range Are Toxic to a Variety of Cells in Vitro. *Exp. Biol. Med. (Maywood)* **2010,** *235*, 741−750.

(63) Maret, W. Zinc in Cellular Regulation: The Nature and Significance of "Zinc Signals". *Int. J. Mol. Sci.* **2017,** *18,* 2285.

(64) Murakami, M.; Hirano, T. Intracellular Zinc Homeostasis and Zinc Signaling. *Cancer Sci.* **2008,** *99*, 1515−22.

(65) Komatsu, K.; Kikuchi, K.; Kojima, H.; Urano, Y.; Nagano, T. Selective Zinc Sensor Molecules with Various Affinities for Zn^{2+}, Revealing Dynamics and Regional Distribution of Synaptically Released Zn^{2+} in Hippocampal Slices. *J. Am. Chem. Soc.* **2005,** *127*, 10197−10204.

(66) Cen, D.; Ge, Q.; Xie, C.; Zheng, Q.; Guo, J.; Zhang, Y.; Wang, Y.; Li, X.; Gu, Z.; Cai, X. ZnS@BSA Nanoclusters Potentiate Efficacy of Cancer Immunotherapy. *Adv. Mater.* **2021,** *33*, 2104037.

(67) Liu, Z.; Zhang, L.; Cui, T.; Ma, M.; Ren, J.; Qu, X. A Nature-Inspired Metal-Organic Framework Discriminator for Differential Diagnosis of Cancer Cell Subtypes. *Angew. Chem. Int. Ed.* **2021,** *60*, 15436−15444.

(68) Nowosad, A.; Jeannot, P.; Callot, C.; Creff, J.; Perchey, R. T.; Joffre, C.; Codogno, P.; Manenti, S.; Besson, A. P27 Controls Ragulator and Mtor Activity in Amino Acid-Deprived Cells to Regulate the Autophagy-Lysosomal Pathway and Coordinate Cell Cycle and Cell Growth. *Nat. Cell Biol.* **2020,** *22*, 1076−1090.

(69) Xu, W.; Erzurum, S. C. Endothelial Cell Energy Metabolism, Proliferation, and Apoptosis in Pulmonary Hypertension. *Compr. Physiol.* **2011,** *1*, 357−372.

(70) Kang, H. M.; Park, B. S.; Kang, H. K.; Park, H. R.; Yu, S. B.; Kim, I. R. Delphinidin Induces Apoptosis and Inhibits Epithelial-to-Mesenchymal Transition Via the ERK/p38 MAPK-Signaling Pathway in Human Osteosarcoma Cell Lines. *Environ. Toxicol.* **2018,** *33*, 640−649.

(71) Slattery, M. L.; Lundgreen, A.; Wolff, R. K. Dietary Influence on MAPK-Signaling Pathways and Risk of Colon and Rectal Cancer. *Nutr. Cancer* **2013,** *65*, 729−738.

(72) Evan, G. I.; Vousden, K. H. Proliferation, Cell Cycle and Apoptosis in Cancer. *Nature* **2001,** *411*, 342−348.

(73) He, T. S.; Ji, W.; Zhang, J.; Lu, J.; Liu, X. ALG-2 Couples T Cell Activation and Apoptosis by Regulating Proteasome Activity and Influencing Mcl1 Stability. *Cell Death Dis.* **2020,** *11*, 5.

(74) Komatsu, N.; Kajiya, M.; Morimoto, S.; Motoike, S.; Yoshii, H.; Iwata, T.; Ouhara, K.; Matsuda, S.; Mizuno, N.; Kurihara, H. Cox2-Mediated PGE2 Production via p38/JNK-c-fos Signaling Inhibits Cell Apoptosis in 3D Floating Culture Clumps of Mesenchymal Stem Cell/Extracellular Matrix Complexes. *Biochem. Biophys. Res. Commun.* **2020,** *530*, 448−454.

(75) Wisdom, R.; Johnson, R. S.; Moore, C. C-Jun Regulates Cell Cycle Progression and Apoptosis by Distinct Mechanisms. *EMBO J.* **1999,** *18*, 188−197.

(76) Takai, Y.; Matikainen, T.; Jurisicova, A.; Kim, M. R.; Trbovich, A. M.; Fujita, E.; Nakagawa, T.; Lemmers, B.; Flavell, R. A.; Hakem, R.; Momoi, T.; Yuan, J.; Tilly, J. L.; Perez, G. I. Caspase-12 Compensates for Lack of Caspase-2 and Caspase-3 in Female Germ Cells. *Apoptosis* **2007,** *12*, 791−800.

(77) Wang, L.; Wei, Y.; Yan, Y.; Wang, H.; Yang, J.; Zheng, Z.; Zha, J.; Bo, P.; Tang, Y.; Guo, X.; Chen, W.; Zhu, X.; Ge, L. CircDOCK1 Suppresses Cell Apoptosis Via Inhibition of miR-196a-5p by Targeting BIRC3 in OSCC. *Oncol. Rep.* **2018,** *39*, 951−966.

(78) Fu, Q.; Qin, T.; Chen, L.; Liu, C. J.; Zhang, X.; Wang, Y. Z.; Hu, M. X.; Chu, H. Y.; Zhang, H. W. miR-29a Up-regulation in AR42J Cells Contributes to Apoptosis via Targeting TNFRSF1A Gene.

World J. Gastroenterol. **2016,** *22*, 4881−4890.

(79) Guo, D.; Du, Y.; Wu, Q.; Jiang, W.; Bi, H. Disrupted Calcium Homeostasis Is Involved in Elevated Zinc Ion-Induced Photoreceptor Cell Death. *Arch. Biochem. Biophys.* **2014,** *560*, 44−51.

(80) Zhang, H.; Duan, J.; Qu, Y.; Deng, T.; Liu, R.; Zhang, L.; Bai, M.; Li, J.; Ning, T.; Ge, S.; Wang, X.; Wang, Z.; Fan, Q.; Li, H.; Ying, G.; Huang, D.; Ba, Y. Onco-miR-24 Regulates Cell Growth and Apoptosis by Targeting BCL2L11 in Gastric Cancer. *Protein Cell* **2016,** *7*, 141−151.

(81) Ranjan, K.; Waghela, B. N.; Vaidya, F. U.; Pathak, C. Cell-Penetrable Peptide-Conjugated Fadd Induces Apoptosis and Regulates Inflammatory Signaling in Cancer Cells. *Int. J. Mol. Sci.* **2020,** *21*, 6890.

(82) He, G.; Pan, X.; Liu, X.; Zhu, Y.; Ma, Y.; Du, C.; Liu, X.; Mao, C. HIF-1α-Mediated Mitophagy Determines ZnO Nanoparticle-Induced Human Osteosarcoma Cell Death Both in Vitro and in Vivo. *ACS Appl. Mater. Interfaces* **2020,** *12*, 48296−48309.

(83) Wang, X.; Lu, X.; Zhu, R.; Zhang, K.; Li, S.; Chen, Z.; Li, L. Betulinic Acid Induces Apoptosis in Differentiated PC12 Cells Via Ros-Mediated Mitochondrial Pathway. *Neurochem Res.* **2017,** *42*, 1130−1140.

(84) Liu, J.; Yuan, X.; Deng, L.; Yin, Z.; Tian, X.; Bhattacharyya, S.; Liu, H.; Luo, Y.; Luo, L. Graphene Oxide Activated by 980 nm Laser for Cascading Two-Photon Photodynamic Therapy and Photothermal Therapy against Breast Cancer. *Appl. Mater. Today* **2020,** *20*, 100665.

(85) Pérez-Hernández, M.; Del Pino, P.; Mitchell, S. G.; Moros, M.; Stepien, G.; Pelaz, B.; Parak, W. J.; Gálvez, E. M.; Pardo, J.; de la Fuente, J. M. Dissecting the Molecular Mechanism of Apoptosis During Photothermal Therapy Using Gold Nanoprisms. *ACS Nano* **2015,** *9*, 52−61.

(86) Zhao, Y.; Zhao, T.; Cao, Y.; Sun, J.; Zhou, Q.; Chen, H.; Guo, S.; Wang, Y.; Zhen, Y.; Liang, X.-J. Temperature-Sensitive Lipid-Coated Carbon Nanotubes for Synergistic Photothermal Therapy and Gene Therapy. *ACS Nano* **2021,** *15*, 6517−6529.

(87) Huang, X.; Zhang, W.; Peng, Y.; Gao, L.; Wang, F.; Wang, L.; Wei, X. A Multifunctional Layered Nickel Silicate Nanogenerator of Synchronous Oxygen Self-Supply and Superoxide Radical Generation for Hypoxic Tumor Therapy. *ACS Nano* **2022,** *16*, 974−983.

(88) Zhao, H.; Xu, J.; Wang, Y.; Sun, C.; Bao, L.; Zhao, Y.; Yang, X.; Zhao, Y. A Photosensitizer Discretely Loaded Nanoaggregate with Robust Photodynamic Effect for Local Treatment Triggers Systemic Antitumor Responses. *ACS Nano* **2022,** *16*, 3070−3080.

(89) Chen, G.; Xu, Q.; Feng, Z.; Xu, Q.; Zhang, X.; Yang, Y.; Zhang, Y.; Liang, X.-J.; Yu, Z.; Yu, M. Glutamine Antagonist Synergizes with Electrodynamic Therapy to Induce Tumor Regression and Systemic Antitumor Immunity. *ACS Nano* **2022,** *16*, 951−962.

(90) Geng, P.; Yu, N.; Macharia, D. K.; Meng, R.; Qiu, P.; Tao, C.; Li, M.; Zhang, H.; Chen, Z.; Lian, W. MOF-Derived CuS@Cu-MOF Nanocomposites for Synergistic Photothermal-Chemodynamic-Chemo Therapy. *Chem. Eng. J.* **2022,** *441*, 135964.

(91) Zhou, J.; Wang, K.; Ding, S.; Zeng, L.; Miao, J.; Cao, Y.; Zhang, X.; Tian, G.; Bian, X.-w. Anti-Vegfr2-Labeled Enzyme-Immobilized Metal-Organic Frameworks for Tumor Vasculature Targeted Catalytic Therapy. *Acta Biomater.* **2022,** *141*, 364−373.